## Reply to referee #1

We thank Referee #1 for reviewing the manuscript and the valuable comments and suggestions which we address below. The responses to the referee comments are given in blue italic letters.

The authors present an analysis of remote sensing retrievals that were collected during several marine cold-air outbreak (MCAO) flights over the Norwegian Sea. Retrievals are based on passive hyper-spectral and polarization measurements in the shortwave spectrum. Translated into a quasi-Lagrangian framework, the retrievals generally show a progressive deepening of the marine boundary layer and an increasing ice fraction with greater distance from the pack ice. The various MCAO strengths covered by the flights show more intense deepening and greater ice fractions for stronger MCAOs. The paper is generally well-written. However, there are a few concerns that the authors should address before the paper is published. I recommend returning the paper for major revisions.

### Major concerns

Quality issues because of sea ice – In several instances the authors write that sea ice impacts the retrieved cloud properties, but it's not 100% clear which data points in the figures are affected. I think the authors should mark suspicious values (e.g., using a different color) in all figures. Also, looking at case "20220404" in Fig. 1, there are substantial flight portions above sea ice, but lines in Fig. 5 and 6 are uninterrupted (and without artifacts); I'm not sure at which times and distances these portions are, but it would be helpful to highlight them.

*Thank you very much for noting this issue. In fact, only the retrieved cloud fraction and ice fraction are (partly) affected by sea ice and this issue only applies to measurements in the marginal ice zone. Other retrieved quantities and measurements outside the marginal ice zone are not impacted. The cloud fraction and ice fraction both rely on the cloud mask from the measurements of the polarization-resolving cameras, which are sensitive to the visible wavelength range only. Detecting clouds in the presence of sea ice (especially in the marginal ice zone) correctly is a well known issue in passive remote sensing. We applied a sea ice mask to focus on measurements above open ocean only to avoid additional uncertainties due to the influence of the surface and to filter the most uncertain data. Nevertheless, some outliers still remained in the data. The threshold value of 80% was chosen as a compromise between avoiding artifacts and not excluding the important very initial phase of the cloud evolution. Small variations of this threshold value did not significantly affect the results, but added or removed outliers and smaller or larger portions of the measurements of the very initial evolution.*
*The lines in Fig. 5 and 6 show composites of the measurements as a function of time and distance above open ocean, which were computed using the backward trajectories. These are not directly measured time series. Excluding parts of the flight tracks due to sea ice does therefore not necessarily lead to gaps in the composites. Some of the lines in these figures are interrupted, if the respective parts of the evolution were not sampled by the flight track. The sea ice mask to filter the data worked better in some cases than in others, which is why more or less outliers are visible in the data of the different flights. This can, for example, be due to the much coarser resolution of the sea ice data of 1km (which is the highest available resolution) compared to the 10 to 100m resolution of the specMACS measurements.*
*We adjusted Fig. 1 to show, which parts of the flight were excluded due to sea ice and which parts were evaluated. In addition, we extended and rewrote the discussion of the sea ice mask in Sect. 2.1. Moreover, we added the exact times and distances of the outliers to the discussion throughout the paper draft to make clearer, which data points are affected. For all changes, please see the Latexdiff.*

Retrieval assumptions – The authors retrieve many cloud microphysical properties and it's not 100% clear if retrieval assumptions are important to do so. For example, are these retrieval look-up-table (LUT) based and what were the assumed cloud vertical structures when generating the LUT (e.g., was liquid always assumed to be above frozen condensate)? The authors should clarify these structural assumptions in Section 2.1. Furthermore, the authors use several thresholds (e.g., for cloud fraction, the watershed algorithm, and thermodynamic phase, etc.). The authors should quantify the sensitivity to these thresholds. For example, for cloud cover the modelling community often uses a cloud-optical depth > 2 or 2.5; which value was chosen here and would slightly different values substantially alter the results?

*Thank you very much for noting that. We rewrote Section 2.1 and added more details to the different retrievals, their assumptions, thresholds, and uncertainties. Please see the Latexdiff for all changes.*
*The cloud top height is derived using a stereographic retrieval and therefore not dependent on threshold values, look-up tables, or forward operators. A detailed validation based on model data was performed by Volkmer et al. (2024).*
*The cloud fraction was calculated using the cloud mask by Pörtge et al. (2023), which depends on the brightness of the observed clouds. Of course, the choice of the threshold value to distinguish between cloudy and cloud-free pixels affects the absolute value of the derived cloud fraction. This is a known issue for cloud masks based on passive remote sensing. Variations of the threshold value shift the derived cloud fraction to smaller or larger values, but measurements closer and further away from the sea ice edge are influenced similarly such that the presented analysis of the temporal and spatial evolution is not affected significantly.*
*Since the retrieval of the horizontal cloud extent is the only retrieval which is not published in a separate paper, we added a detailed description of the retrieval method to the appendix.*
*The liquid cloud droplet size is obtained from the cloudbow retrieval. It is based on multi-angle polarization measurements of the cloudbow, which is formed by single scattering on (spherical) liquid cloud droplets. The droplet size is derived by fitting polarized scattering phase functions according to Mie theory to the measurements. The retrieval was validated based on synthetic data in Volkmer et al. (2024) and an additional analysis based on synthetic measurements showed that the influence of cloud ice on the cloudbow retrieval is negligible for ice fractions smaller than 0.8.*
*The spectral ice index is directly obtained from the data by computing the spectral slope of the radiance measurements and no look-up tables or forward operators are needed. The threshold value of 20 was not applied in the retrieval but is only used to interpret the results. This threshold value was derived from radiative transfer simulations in Ehrlich et al. (2008,2009), which showed that the ice index values split up between liquid water clouds and mixed-phase or ice clouds with a threshold value of 20 distinguishing the two groups.*
*The polarized optical ice fraction instead is obtained by fitting multi-angle polarization measurements from a forward operator to measurements. The forward operator assumes homogeneously mixed clouds. The deviation of the actual vertical ice fraction profile from this assumptions leads to an additional uncertainty. However, based on passive remote sensing, no information about the vertical ice fraction profile can be obtained such that assumptions have to be made. The uncertainty introduced by this and other assumptions was characterized in detail in Weber et al. (2025b).*

Value for the wider community – While cloud-top height and cloud cover are common properties that can be directly used in the modeling community, I'm less sure how to translate the other quantities and think the authors should discuss it. For example, ice index and ice fraction inform on various layers near the cloud-top; how would it be comparable to other measurements (e.g., in-situ cloud probes) or model output? Specifically for model output, would a forward simulator be needed?

*A forward operator is actually only needed to compare the ice index to model output. All other variables can usually directly be computed from the model output. In particular, for the ice fraction and effective radius of liquid cloud droplets, retrieved quantities from synthetic measurement data using LES simulations have already been compared to the model values to validate the retrievals in*

*Volkmer et al. (2024) and Weber et al. (2025b).*
*The comparison to other measurement data is more difficult. First, a very good collocation of remote sensing and in situ measurements is necessary. For a direct comparison, the in situ measurements additionally would have to be collected at the correct altitude close to cloud top, which is very difficult. However, a more statistical comparison is possible. Pseudo-vertical profiles of microphysical quantities can be derived from the specMACS measurements (see for example our second paper Weber et al. (2025a)). These profiles could be compared to vertical profiles measured with in situ probes. Unfortunately, during HALO-(AC)³ in situ measurements were only collected at a very limited number of constant flight levels. The effective radius of liquid cloud droplets can be measured with different in situ probes. For the ice fraction, the optical thickness of liquid water and ice has to be computed from measurements of the droplet and ice crystal size and the liquid water content and ice water content, such that an equivalent optical ice fraction can be derived from the in situ measurements. The qualitative ice index, however, cannot directly be compared to in situ measurements. In Weber et al. (2025a) we show a (qualitative) comparison to radar and lidar observations and combine in situ and remote sensing observations to further investigate microphysical properties and processes in the observed mixed-phase clouds. We added more information about how to compare the retrieved quantities to model output to the discussion: "The macrophysical cloud properties, such as the cloud top height, can directly be derived from typical model output and be compared to measurements. In addition, the ice fraction and effective radius of liquid cloud droplets can be computed from model output as described in Volkmer et al. (2024) and Weber et al. (2025b). A forward operator is only needed for a direct comparison of modeled and measured ice indices, as the ice index is a qualitative measure of the cloud thermodynamic phase and computed from measured radiances. … Weber et al. (2025a) also includes a comparison to active remote sensing observations and additionally applies collocated in situ observations."*

**Minor concerns**

ll. 35-38 I'm not sure that this vertical structure applies to MCAO clouds that are rather convective.

*Thank you very much for noting that. The cited reference discusses Arctic mixed-phase clouds in general without the specific focus on MCAOs. Therefore, we changed the sentence to "Arctic mixed-phase clouds have a typical vertical structure". However, radar and lidar data as well as passive remote sensing observations during HALO-(AC)³ actually also indicate a more liquid-dominated layer at the cloud top for the observed MCAO mixed-phase clouds, as discussed in the second part of this work (Weber et al., 2025) and in Schirmacher et al. (2024). In addition, liquid cloud tops during MCAOs were also observed by Geerts et al. (2022).*

ll. 40-41 I'm not sure how relevant the WBF process is inside MCAOs but would probably guess that riming is the dominant mixed-phase process.

*We added riming as a second mixed-phase processes here.*

l. 107 Do both instruments cover the same range?

*Yes, the field of view of the spectrometers is completely covered by the polarization-resolving cameras, which have a larger field of view. We added this information.*

l. 124 Are the results sensitive to this threshold (also see second major point).

*The results are not significantly affected by this threshold. See the discussion above.*

Fig. 2: It would be useful to list the case date in the caption or somewhere in the figure.

*We added the date in the caption of Fig. 2 to 4 as suggested.*

Fig. 3 and 4: Maybe add uncertainty around each line (e.g. from percentiles).

*We added uncertainty in terms of standard deviation to Fig. 2 and 4 as suggested.*

l. 288 Cloud-top height in “20220401” does not appear that high?

*The cloud top height on 20220401 increased from around 200m to about 1700m. During other flights we see an increase until up to 2500m. We changed the sentence to: “The cloud top height in panels (a) and (d) increases with time and distance from the ice edge from a few hundred meters to a maximum of about 2.5km, depending on the research flight”.*

Fig. 5: The cloud radius of “20220329” seems small. Is the mean value perhaps a poor representative here?

*According to the satellite image and the specMACS observations, the cloud size on 20220329 is similar to the other research flights. This is also reflected in Fig. 5c and f, where the cloud radius shows generally values in a similar range as the other flights.*

ll. 230-231 Related to the exclusion of high solar zenith angles: Do higher angles also mean less vertical penetration into the cloud? I think it would be good to provide approximate penetration depth for all cases (and all distances and times).

*Observations at larger solar zenith angles are not possible, since the solar and viewing geometry do not allow for the observation of the cloudbow angular range within the field of view of the polarization-resolving cameras, such that the ice fraction and cloud droplet size could not be derived. So, we did not exclude any existing data here, but there is no data available. We changed the sentence to: “For later times (after approx. 210min), no measurements of the effective radius and the ice fraction are available because the solar zenith angle during this part of the flight was too large for the cloudbow to be observed inside the field of view of the cameras, such that the retrievals could not be applied.”*
*Moreover, we added information about the penetration depth to Sect. 2.1 (see above). The vertical penetration depth varies depending on the solar zenith angle. The signal location for the retrieved ice fraction was analyzed in detail in Weber et al. (2025b) and varied between about 1 and 2 depending on the solar zenith angle. We also checked the variation of the solar zenith angle during the research flight but did not find a correlation between the solar zenith angle variation and the variation of the cloud properties.*

**Typos**

l. 244 Please check this sentence. Can uncertainty be negative and does the uncertainty have an uncertainty?

*We added the information about the uncertainties to Sect. 2.1 and changed the sentences to avoid confusion. The given values indicated the mean and standard deviation of the differences between the simulated and retrieved droplet radii in the model-based evaluation.*

## Reply to referee #2

We thank Referee #2 for reviewing the manuscript and the valuable comments and suggestions which we address below. The responses to the referee comments are given in blue italic letters.

**General**

This manuscript analyzes observations and retrievals of cloud macrophysical and microphysical properties during the HALO-(AC)³ field campaign, focusing on their temporal and spatial variations. One case out of six is used to demonstrate detailed cloud evolution, while the statistical analysis shows the spread and general tendencies across all six cases. The presented dataset is valuable for improving our understanding of MCAO cloud structures and their evolution.

However, the selection of the demonstration case needs stronger justification. In addition, when comparing the aircraft-based findings with previous studies, especially satellite-based analyses, the manuscript should provide clearer explanations for why the results differ. Simply stating that satellite resolution is coarse or retrieval uncertainty is high is not sufficient to explain contrasting trends.

I also find that the statistical analysis section does not add much new information beyond what is already shown in the case study, except for illustrating the spread among cases. Based on these concerns, I recommend returning the manuscript to the authors for major revision before it can be considered for publication in ACP.

**Major Comments**

1. Case selection (Section 3.1)

Please justify the choice of the 20220401 case as the main demonstration of cloud macrophysical and microphysical evolution. Based on Figure 1, this case does not appear to be the most representative of a classic MCAO. In this case, cloud streets are oriented roughly parallel to the ice edge, implying continuous advection of fresh cold air from the ice to the open ocean. As a result, cloud properties are persistently influenced by cold, dry air.

A more typical MCAO would involve cold air flowing off the ice edge and clouds forming with roll structures oriented roughly perpendicular to the ice edge (e.g., 20220329). While the 20220401 case may still provide useful insights, its findings may lack generality. This might explain why the cloud fraction evolution in this case differs from the statistical behavior reported in Murray-Watson et al. (2023). In your Figure 5, the 20220401 case appears to be the only one with nearly constant cloud fraction during the first several hours, and it also has the shortest flight time over open ocean.

*The MCAO observed on 20220401 was the strongest MCAO sampled during HALO-(AC)$^3$. Based on the MCAO index, it was a typical event for this region and time of the year (Walbröl et al., 2024). The flight was selected because there was a clear northerly flow on that day with air masses originating from the central Arctic. In contrast, the other observed MCAOs were much more influenced by the topography of Svalbard or showed more complicated, rather circular backward trajectories. In addition, collocated in situ measurements are available for the flight on that day and a large number of dropsondes was released. This was not the case for the other flights. Other studies also investigated specifically the research flight on 20220401 and we wanted to contribute to a complete picture of the MCAO observed on that day. Therefore, we also selected this flight for a more detailed case study. In addition, the second part of this work in Weber et al. (2025a) discusses the vertical cloud structure on that day using the collocated in situ measurements. We agree that the cloud streets are not entirely perpendicular to the sea ice edge, which might influence the cloud evolution*

*compared to a MCAO with the mean wind direction aligned entirely perpendicular to the sea ice edge, and added this information to the discussion of the results. However, the conditions were typical for a MCAO in this region during that time of the year, as discussed by Walbröl et al. (2024) and Kirbus et al. (2024). We added more details about the case selection to Sect. 3:*
*"The event on 2022-04-01 was the strongest MCAO sampled during HALO-(AC)$^3$. In contrast to the other MCAO flights, the backward trajectories showed a clear northerly flow from the central Arctic towards the South without a significant influence of the topography of the island of Svalbard. In addition, collocated in situ measurements were collected on this day. Several studies have already analyzed data from the research flight on 2022-04-01. Kirbus et al. (2024) studied the thermodynamic evolution during this MCAO, based on dropsonde measurements during HALO-(AC)$^3$. In addition, Schirmacher et al. (2024) investigated the roll convection regime using radar observations. In the following, the temporal and spatial evolution of macrophysical and microphysical cloud properties, including cloud top height, cloud thermodynamic phase, and cloud droplet size, derived from passive remote sensing with specMACS will be presented and discussed. This complements existing studies about the MCAO observed on 2022-04-01 and contributes towards a complete picture of this case. The second part of this work (Weber et al., 2025a) additionally analyzes the vertical cloud structure observed on this day, exploiting the collocated remote sensing and in situ observations and building upon the results presented in the following."*

2. Comparison with previous studies

Both the case study and the statistical analysis are compared with previous work, especially Murray-Watson et al. (2023, hereafter MW23). However, it is not a fair comparison to contrast a single case with a statistical composite from many cases, particularly when the selected case is not a typical MCAO example.

For cloud fraction, you attribute differences between your results and MW23 to instrument resolution (L212–215). It is not clear how resolution alone would systematically change cloud fraction estimates and the temporal/spatial trend, and this needs clearer explanation. Later, you note that stronger MCAOs tend to have higher cloud fractions, consistent with MW23.

For cloud particle size, MW23 found smaller sizes for stronger MCAOs, which is opposite to your result. You attribute this partly to satellite retrieval uncertainties, but it is unclear why such uncertainties would specifically lead to smaller effective radii in stronger MCAOs. Wouldn't retrieval uncertainty affect strong and weak MCAO cases similarly? This point needs more careful physical and methodological explanation.

*Thank you very much for this comment. We changed the discussions in sections 3.1 to make clearer that 2022-04-01 is a single case study and might therefore differ from the average general statistics in Murray-Watson et al. (2023). In addition, we added more comparisons to other references and more explanations about the observed results and potential reasons for differences between the different works to both sections 3.1 and 3.2. In particular, we adjusted the parts discussing the differences between the observed cloud fractions and cloud droplet effective radii between our work and Murray-Watson et al. (2023). Differences between the instrument resolutions as well as the choice of threshold values can affect the absolute values of the derived cloud fraction. We agree that this applies similarly to weak and strong cold air outbreaks and see, in general, a similar behavior of weak and strong MCAOs as Murray-Watson et al. (2023). An explanation for the observed almost constant cloud fraction on 2022-04-01 compared to the general statistics could, for example, be that this individual case is not entirely representative as mentioned by you. Regarding the cloud droplet radii, there are different potential reasons for differences in the absolute values, including different retrieval methods, sensitivities, and instrument resolutions. The observed differences in the droplet size during strong and weak cold outbreaks which are opposite to the findings of Murray-Watson et* *al. (2023) can also have several reasons. First, variations in aerosol concentrations can have a large influence on the cloud droplet size. Second, during HALO-(AC)³, only six MCAOs could be observed, which showed a large variability and occurred in different regions under different synoptic situations. Nevertheless, these six events are not necessarily representative for the general statistics of weak and strong MCAOs. For all changes please see the Latexdiff.*

3. Relationship between Sections 3.1 and 3.2

I understand that Section 3.1 presents a detailed case and Section 3.2 presents statistics. However, Section 3.2 does not seem to add much new information beyond Section 3.1, other than showing the large spread across cases. These two sections could potentially be merged, with individual cases discussed in the context of the statistics.

I briefly looked at your Part 2 manuscript on vertical cloud structure. Combining horizontal and vertical structures into a single comprehensive observational paper could be very valuable. As it stands, the current manuscript alone does not seem sufficient as a standalone paper. I will leave it to the authors to decide.

If you prefer to keep this as a separate paper, I suggest adding more discussion of the physical mechanisms behind the observed temporal and spatial evolution. Currently, the manuscript mostly presents observations, with limited interpretation. Alternatively, you could emphasize which of your findings are truly new compared to previous satellite or modeling studies.

*The first draft was actually a single paper including the analyses of the temporal and spatial cloud evolution as well as the vertical cloud structure. However, the draft was very long and addressed many different research questions relevant also to slightly different communities. Therefore, we decided to split the draft in to two parts, since shorter papers are usually also easier to read. The second paper got a positive review so far and we would, therefore, like to keep the two separate paper drafts. However, we agree that this paper draft is comparably short. We followed your suggestions and added more discussions, explanations, and interpretations about the observed temporal and spatial evolution throughout the paper and additionally emphasized more which of our findings are new. An explanation, why we show the case study in addition to the statistics is given above in the answer to the first comment. With the statistics, we wanted to go beyond a simple case study and discuss the observed variability as well as differences depending on the MCAO intensity. Studies based on airborne observations often only discuss single case studies. Then, often the question of the representativity and poor statistics is raised. Therefore, we analyzed all available data. For all changes please see the Latexdiff.*

**Minor Comments**

L50: can you elaborate briefly on why true Lagrangian observations are challenging.

*We added a brief explanation: "In the Arctic, no geostationary satellite data is available and aircraft move much faster than the observed airmass."*

L78: "aircraft" -> "aircrafts."

*Changed as suggested.*

L105: The full name of the instrument should be given at its first appearance.

*Changed as suggested.*

Figure 2: What does “WGS84” on the y-axis of the left column mean? Has this been defined?

*WGS84 refers to the World Geodetic System 1984 and specifies the reference system defining the Earth’s surface and therefore the cloud top height. We included this information for completeness since some studies use ellipsoidal and others geoid heights. We added an explanation: “The cloud top heights are given above the World Geodetic System 1984 (WGS84) ellipsoid.”*

L208–209: You state that cloud fraction remains almost constant during the first hours. To me, the variability in the first half looks comparable to that in the second half, as seen in Figures 2b and 2e. Please clarify how this conclusion is reached.

*The “almost constant” referred to the mean cloud fraction, which remains similar. We agree that the variability is large and also remains almost constant with time. We changed the sentence to: “The average cloud fraction (see Fig. Fig2b and 2e) remained almost constant during the first hours of the observed MCAO, as can also be seen in the RGB images in Fig. 3. The variability of the cloud fraction is high showing values between 0.5 and 0.8 and is also almost constant with time.”*

L212–215: MW23 presents statistics from many MCAO cases, while you compare their results with a single case. I suggest avoiding direct comparison of one case with statistical composites. Also, while specMACS may provide more accurate cloud identification due to higher resolution, it may also have a narrower field of view than satellites, which could affect cloud fraction estimates.

*We changed and extended the comparisons between different studies. Please see our answer to major point 2 above.*

Figure 4: There is a distance near the beginning where no data appear in the bottom row, while data are shown in the top row once the aircraft is over open ocean. Please clarify why this occurs.

*Both rows show the same measurements, but the upper row displays them as a function of time above open ocean and the bottom row as a function of distance above open ocean. Time and distance were both calculated using the same backward trajectories. However, the wind speed is not necessarily constant along the trajectories which leads to differences between the visualizations in terms of time and distance. In particular, close to the sea ice edge, the surface wind typically increases due to the off-ice acceleration which leads to a “stretching” of the curves at small distances above open ocean compared to small times above open ocean. This information was given in the section before and we extended it to: “The different shapes of the curves describing, e.g., the evolution of the cloud top height during the first kilometers above open ocean compared to the first minutes above open ocean in Fig. 2 and similar figures in the following sections can be explained by changing wind speeds due to the off-ice acceleration at the sea ice edge.”*

# Quasi-Lagrangian observations of cloud transitions during the initial phase of marine cold air outbreaks in the Arctic – Part 1: Temporal and spatial evolution

Anna Weber[1], Benjamin Kirbus[2,3], Manfred Wendisch[2], and Bernhard Mayer[1]

[1]Meteorologisches Institut, Ludwig-Maximilians-Universität München, Munich, Germany
[2]Leipziger Institut für Meteorologie (LIM), Universität Leipzig, Leipzig, Germany
[3]Fraunhofer-Institut für Energiewirtschaft und Energiesystemtechnik (IEE), Kassel, Germany

**Correspondence:** Anna Weber (Weber.Ann@physik.uni-muenchen.de)

**Abstract.** This work aims to quantify the macrophysical and microphysical properties of Arctic mixed-phase clouds and their temporal and spatial evolution during marine cold air outbreaks in the Arctic. In particular, cloud thermodynamic phase partitioning and phase transitions are discussed. To this end, high-resolution observations from the airborne hyperspectral and polarized imaging system specMACS during the HALO–$(\mathcal{AC})^3$ campaign are analyzed within a quasi-Lagrangian framework based on backward airmass trajectories. Six flights targeting marine cold air outbreaks of different intensity are compared to investigate the variability of cloud evolutionand its dependence on the cold air outbreak intensity. With increasing time the airmass spent above open, sea ice-free ocean, rising cloud top heights, increasing horizontal cloud extents, and growing effective radii of liquid cloud droplets are reported observed for all cases. In addition, a phase transition from the liquid water to the mixed-phase cloud regime is detected and the ice fraction increases with time. The variability between the observed cloud properties during the cold air outbreaks is large. Larger and faster increasing cloud top heights and effective radii of liquid cloud droplets are observed during stronger events. In addition, the phase transition from the liquid water to the mixed phase occurs earlier and higher larger ice fractions are reached during the more intense events. The presented data and analyses provide unique observational data, which can be used to improve the representation of low-level Arctic mixed-phase clouds and their evolution during marine cold air outbreaks in models in the future.

## 1 Introduction

During marine cold air outbreaks (MCAOs) in the Arctic, cold and dry airmasses are advected over the cold sea ice towards warm open ocean (Papritz and Spengler, 2017; Fletcher et al., 2016). The temperature difference between the cold advected advected cold airmasses and the ocean surface can be up to reach 30 K (Papritz and Spengler, 2017). These large enormous horizontal temperature gradients create large vertical surface energy fluxes (sensible and latent heat), intense turbulence, and large heat and moisture fluxes, which may contribute to about 60 % to 80 % of oceanic heat loss during winter in the Nordic Seas, and may affect additionally deep water formation and sea ice evolution (Papritz and Spengler, 2017; Svingen et al., 2023). In additionFurthermore, the strong horizontal temperature gradients between the sea ice surface and ocean skin temperatures

~~lead to~~ promote convection and the formation of low-level clouds (Papritz and Spengler, 2017). The clouds related to MCAOs typically organize into cloud streets oriented along the mean wind direction, ~~and transition~~ which transform into cellular structures further downstream due to a decoupling of the atmospheric boundary layer (ABL) and accompanying precipitation formation (Brümmer, 1999; Gryschka and Raasch, 2005; McCoy et al., 2017; Abel et al., 2017; Pithan et al., 2018; Tornow et al., 2021). With increasing time and distance from the formation location of the MCAO, the ABL typically deepens from a few hundred meters to approximately 1 km to 2 km (Brümmer, 1996). MCAOs are most frequently occurring in winter, but also evolve in spring and autumn (Fletcher et al., 2016). They may be related to severe weather events ~~reaching into~~ impacting the mid-latitudes, including extremely cold periods and heavy snowfall, and ~~to~~ they may initiate polar lows (Pithan et al., 2018). The Fram Strait is one of the main pathways of MCAOs in the Arctic and intense MCAOs are frequently observed in this region (Papritz and Spengler, 2017; Dahlke et al., 2022).

Large-scale as well as high-resolution models are struggling to correctly represent the airmass transformations during meridional transports into and out of the Arctic (Sato et al., 2016; Pithan et al., 2016; Tomassini et al., 2017; Field et al., 2017; Wendisch et al., 2021). Especially the microphysical evolution of clouds during MCAOs is difficult to model (Pithan et al., 2014; McCoy et al., 2015; Tan and Storelvmo, 2019; Field et al., 2014; Abel et al., 2017). Consequently, future projections of Arctic climate properties are uncertain (Smith et al., 2019; Cohen et al., 2020; Block et al., 2020).

The clouds formed during MCAOs are ~~typically~~ commonly of a mixed-phase type~~and~~. Arctic mixed-phase clouds have a typical vertical structure. A geometrically thin layer containing supercooled liquid water droplets is located at the cloud top from which ice crystals form via heterogeneous nucleation and sediment downwards (Morrison et al., 2012). The cloud thermodynamic phase partitioning and its spatial distribution are important ~~quantities since they affect~~ cloud parameters, impacting the radiative effect of the clouds (Choi et al., 2014; Matus and L'Ecuyer, 2017). ~~The spatial~~ In addition, the distribution of supercooled liquid water ~~and ice influences~~droplets and ice crystals influence, e.g., riming and the efficiency of the Wegener-Bergeron-Findeisen process, which can lead to rapid glaciation of the clouds (Korolev et al., 2017; Korolev and Milbrandt, 2022), and thus affects ~~the~~ cloud cover and ~~cloud~~ lifetime (Pithan et al., 2014). Climate and general circulation models struggle to correctly represent mixed-phase clouds and their microphysical properties (Morrison et al., 2012; Pithan et al., 2014; Komurcu et al., 2014; Cesana et al., 2015, 2022). In particular, the cloud thermodynamic phase partitioning and the vertical distribution of cloud liquid water are challenging for models of different scales (Inoue et al., 2021; Kretzschmar et al., 2019, 2020).

MCAOs and the related clouds have been studied extensively using reanalysis data, ground-based and ship-borne sampling, airborne in situ and remote sensing measurements, satellite observations, as well as model data. Most studies used an Eulerian perspective with a locally fixed coordinate system, while some others applied a quasi-Lagrangian approach. In the Lagrangian perspective, the coordinate system follows the observed airmass, which allows for investigating its temporal evolution. However, ~~real~~ true Lagrangian observations are challenging ~~(Wendisch et al., 2023).~~ if not impossible (Wendisch et al., 2024). In the Arctic, no geostationary satellite data is available and aircrafts move much faster than the observed airmass. Instead, the evolution of airmasses can be studied in a quasi-Lagrangian way by applying backward trajectories (Wendisch et al., 2023, 2025).

Several studies focused on the properties of clouds during MCAOs. These include dedicated ground-based and ship-based field campaigns providing Eulerian observations of cloud properties ~~(Uttal et al., 2002; Geerts et al., 2022; Shupe et al., 2022; Lackner et al~~ (Uttal et al., 2002; Geerts et al., 2022; Shupe et al., 2022; Lackner et al., 2023; Mages et al., 2023; Wendisch et al., 2023; Xia and McFarq . In addition, the microphysical properties of the different cloud regimes during MCAOs and transitions between them were studied during airborne field campaigns using in situ data (Young et al., 2016; Abel et al., 2017; Lloyd et al., 2018; Michaelis et al., 2022) as well as remote sensing observations (Ruiz-Donoso et al., 2020). Besides, model data were applied to investigate the evolution of clouds in MCAOs (Tornow et al., 2021). Quasi-Lagrangian analyses of cloud properties during MCAOs combining satellite observations with backward airmass trajectories were carried out by Murray-Watson et al. (2023), Wu and Ovchinnikov (2022), Tornow et al. (2023), Mateling et al. (2023), and Seppala et al. (2025). These studies investigated the temporal evolution of macrophysical and microphysical cloud properties, as derived from MODIS or CloudSat data, and their ~~dependency~~ dependence on the MCAO strength or aerosol conditions. However, satellite observations of Arctic cloud properties are only possible with polar-orbiting satellites and strongly affected by small-scale variability, which is not resolved by the coarse resolution satellite measurements (Ahn et al., 2018; Marchant et al., 2020). The retrieval of cloud thermodynamic phase partitioning and further cloud microphysical properties is especially challenging, and most satellite-based studies are restricted to liquid water clouds. Typical scales of inhomogeneities in Arctic clouds are on the order of a few hundred meters (Schäfer et al., 2017, 2018). These scales can be resolved by high-spatial resolution airborne measurements. Airborne quasi-Lagrangian observations of MCAO clouds in the Arctic were performed during the HALO–$(\mathcal{AC})^3$ campaign (Wendisch et al., 2024). Even though several airborne research campaigns were conducted in the Arctic during the last decades (Forsberg et al., 2023) and some quasi-Lagrangian airborne measurements were collected outside the Arctic (Boettcher et al., 2021), HALO–$(\mathcal{AC})^3$ appears to be the first airborne campaign using a quasi-Lagrangian sampling strategy in the Arctic. Schirmacher et al. (2024) analyzed the evolution of precipitation and other cloud properties in the roll convection regime using radar data in two case studies of a stronger and a weaker MCAO during HALO–$(\mathcal{AC})^3$. However, the evolution of cloud thermodynamic phase and microphysical cloud properties has not been studied in a quasi-Lagrangian approach using high-resolution airborne measurements so far.

This work is based on measurements of the ~~specMACS instrument (Ewald et al., 2016; Weber et al., 2024)~~ spectrometer of the Munich Aerosol Cloud Scanner (specMACS, Ewald et al., 2016; Weber et al., 2024) during the airborne HALO–$(\mathcal{AC})^3$ field campaign (Wendisch et al., 2024; Ehrlich et al., 2025). ~~HALO–$(\mathcal{AC})^3$ was conducted in March and April 2022. The German High Altitude and LOng range research aircraft (HALO, Krautstrunk and Giez, 2012; Stevens et al., 2019) was based in Kiruna and two further research aircraft (Polar 5 and Polar 6) operated out of Svalbard. The~~ The campaign generally aimed at improving the understanding of airmass transformations during meridional transports into and out of the Arctic~~(Wendisch et al., 2024; Ehrlich et al., 2025). HALO~~ . To this end, the German High Altitude and LOng range research aircraft (HALO, Krautstrunk and Giez, 2012; Stevens et al., 2019) followed a quasi-Lagrangian flight strategy, allowing for studying the evolution of cloud properties during MCAOs. specMACS is a hyperspectral and polarized imaging system operated in a downward-looking perspective on board HALO. It provides high-spatial resolution information about cloud macrophysical and microphysical properties, including quantitative information about cloud thermodynamic phase partitioning.

The objective of this work is to study the temporal and spatial evolution of macrophysical and microphysical properties of clouds during MCAOs in a quasi-Lagrangian way, with a special focus on cloud thermodynamic phase partitioning and phase transitions. Aim is to provide high spatial and temporal resolution data about the evolution of clouds during the initial phase of MCAOs, which can be used for model evaluation to improve the representation of mixed-phase clouds and airmass transformations during MCAOs. Furthermore, the data can help to further our understanding of Arctic mixed-phase cloud processes and, in particular, phase changes in these clouds. For this purpose, measurements of cloud properties from specMACS are combined with backward trajectories. The applied data and methods are introduced in Sect. 2. During HALO–$(\mathcal{AC})^3$, in total six MCAOs were sampled. The cloud evolution is investigated for a strong MCAO in Sect. 3.1. Afterwards, the analyses are extended to all observed cases. The variabiliy between the different observed MCAOs and the dependence of the cloud evolution on the MCAO intensity are discussed in Sect. 3.2. Finally, the results are summarized in Sect. 4. The aim of this work is to provide high spatial and temporal resolution information about the evolution of clouds during the initial phase of MCAOs, which can be used for model evaluation to improve the representation of mixed-phase clouds and airmass transformation during MCAOs. Furthermore, the data can help to further our understanding of Arctic mixed-phase cloud processes and, in particular, phase changes in these clouds. The analyses of the temporal and spatial cloud evolution during MCAOs presented here are extended to the vertical dimension in the second part of this work in Weber et al. (2025a), which investigates the vertical cloud structure and its evolution based on specMACS and other remote sensing and in situ measurements during HALO–$(\mathcal{AC})^3$.

## 2 Data and methods

### 2.1 Measurements

The data used in this work were collected during the airborne HALO–$(\mathcal{AC})^3$ measurement campaign in the Arctic (Wendisch et al., 2024; Ehrlich et al., 2025). The German research aircraft HALO , which was conducted in March and April 2022. The German High Altitude and LOng range research aircraft (HALO, Krautstrunk and Giez, 2012; Stevens et al., 2019), based in Kiruna, was equipped with remote sensing instrumentation and followed a quasi-Lagrangian sampling strategy. In addition, several research flights were performed in coordination with the Polar 5 and Polar 6 aircraft (Wesche et al., 2016), operating out of Svalbard and containing remote sensing and in situ instrumentation. This work, however, focuses on data from HALO.

The analyses presented in the following sections this work are based on measurements of the spectrometer of the Munich Aerosol Cloud Scanner (specMACS, Ewald et al., 2016; Weber et al., 2024)specMACS instrument (Ewald et al., 2016; Weber et al., 2024), which was operated in a downward-looking configuration on board HALO. specMACS consists of two hyperspectral line cameras (so-called VNIR and SWIR), which are sensitive to the visible and near-infrared wavelength range between 400 nm and 2500 nm, and two 2D RGB polarization-resolving cameras. The SWIR spectrometer used in this work has a field of view of 35.3° in across-track direction, and the polarization resolving polarization-resolving cameras have a maximum combined field of view of $91° \times 117°$ in along-track and across-track direction, respectively, covering the entire field of view of the spectrometers. The different components of specMACS provide high-spatial resolution high-spatial-resolution measurements of macrophysical and microphysical properties of clouds cloud properties with spatial resolutions between 10 m and 100 m for at typical flight altitudes (10 km), depending on the retrieved quantity.

Macrophysical cloud properties that can be have been derived from the measurements include the cloud top height, the cloud fraction, and the horizontal extent of the clouds. The cloud top height is obtained from a stereographic retrieval using a the method by Kölling et al. (2019), and the cloud . A model-based evaluation showed a mean difference of 46±140 m between the retrieved and simulated cloud top heights (Volkmer et al., 2024). The cloud fraction is calculated from the brightness-based cloud mask from Pörtge et al. (2023). The cloud mask by Pörtge et al. (2023), which is based on the brightness of the observed clouds. The threshold value distinguishing cloud-free and cloudy pixels is determined using the method by Otsu (1979). Small variations of the threshold value lead to slightly lower or higher cloud fractions but do not significantly change the results presented in the following sections. The horizontal cloud extent is derived from the retrieved 3D cloud geometry obtained from the stereographic retrieval using the watershedding algorithm implemented in the Tracking and Object-Based Analysis of Clouds (TOBAC) package (Heikenfeld et al., 2019; Sokolowsky et al., 2024). The algorithm provides the horizontal area of the identified cloud elements from which an effective cloud radius was calculated by assuming under the assumption of a circular shape. A more detailed description of the derivation of the horizontal cloud extent is provided in Appendix A.

Moreover, specMACS provides measurements of microphysical cloud properties. The effective radius of liquid cloud droplets is computed with the multi-angle polarimetric cloudbow retrieval by Pörtge et al. (2023). The retrieval is based on multi-angle polarization observations of the cloudbow, which is formed by single scattering on liquid cloud droplets, and the retrieved effective radii are thus representative for the cloud top, corresponding to an optical thickness of about 1. The effective radii of the liquid cloud droplets are determined by fitting polarized scattering phase functions according to Mie theory from a look-up table to the observations. The uncertainty of the measured effective radii of liquid cloud droplets from the cloudbow retrieval was characterized based on an evaluation with synthetic data, which showed mean differences between measured and simulated droplet radii of $-0.2 \pm 1.6\,\mu$m (Volkmer et al., 2024; Pörtge, 2024).

Information about the cloud thermodynamic phase is derived from the specMACS measurements following two different approaches based on spectral and polarization measurements, respectively. Firstly, the spectral ice index defined by Ehrlich et al. (2008) and Ruiz-Donoso et al. (2020) was calculated from the radiance measurements of the SWIR spectrometer. The ice index is represents a qualitative measure of the thermodynamic phase . Values smaller than of the cloud particles, exploiting spectral absorption differences between liquid water and ice in the near-infrared which lead to different spectral slopes depending on the thermodynamic phase. The resulting phase index represents the thermodynamic phase at the cloud top. However, the spectral measurements used to calculate the ice index originate from deeper layers within the cloud than the polarization measurements, since the polarization signal is dominated by single scattering. According to sensitivity studies based on radiative transfer simulations, values of the ice index below 20 indicate a liquid water cloudand larger values , values above 20 correspond to a mixed-phase cloud (Ehrlich et al., 2009).

Secondly, a quantitative optical ice fraction was derived from the measurements of the polarization-resolving cameras by applying the polarimetric phase partitioning retrieval introduced by Weber et al. (2025b). The ice fraction is defined as the ratio of the ice optical thickness to the total cloud optical thickness. It is determined by fitting multi-angle polarization signals from a forward operator to polarization measurements. The retrieved ice fractions correspond to the average ice fraction from the cloud top to an optical thickness of about 1 to 2 below the top under the assumption of homogeneously mixed clouds (Weber et al., 2025b). Depending on the observation and cloud geometry, different scattering angle ranges and retrieval configurations can be used. Here, the results of the polarimetric phase retrieval for the cloudbow angular range using the IDEFAX forward operator for the green color channel are shown using the forward operator with the parameterization of 3D cloud geometry are shown, and only observations with saturated polarization signals are considered, because they provide the smallest uncertainties (Weber et al., 2025b). For more details to the phase retrieval, the reader is refered to Weber et al. (2025b) . for Arctic mixed-phase clouds (Weber et al., 2025b). Nevertheless, the results have a high uncertainty, especially when the solar zenith angle is very large. The microphysical cloud properties derived from specMACS observations are representative for the cloud top as they are based on passive remote sensing. The spectral measurements used to calculate the ice index originate from deeper layers within the cloud than the polarization measurements applied to compute the ice fraction and the effective radius of the liquid cloud droplets, since the polarization signal is dominated by single scattering. A detailed discussion of retrieval uncertainties and more details to the phase retrieval can be found in Weber et al. (2025b).

Only measurements above open ocean were considered in the analyses. Over sea ice, the retrievals based on passive remote sensing have are tainted with additional uncertainties due to the influence of the high reflective surface, especially for thin clouds. In addition, it is difficult to challenging to correctly detect clouds above sea icecorrectly. Thus, a sea ice mask . While the stereographic retrieval and the cloudbow retrieval are only negligibly affected due to their particular retrieval methods, sea ice surfaces misidentified as clouds can lead to an overestimation of the retrieved cloud fraction and optical ice fraction in the marginal sea ice zone and above sea ice, since both retrievals rely on the applied cloud mask. The cloud mask for the measurements of the polarization-resolving cameras and hence the optical ice fraction is more strongly affected by sea ice than the cloud mask for the spectral measurements used to compute the spectral ice index. The reason is that the polarization-resolving cameras are sensitive to the visible wavelength range, where sea ice surfaces are bright. In contrast, a wavelength of 1640 nm, where sea ice is comparably dark, was used for the cloud mask of the spectral measurements. To exclude measurements above sea ice and filter the most uncertain measurements, a sea ice mask was computed from the combined AMSR2-MODIS sea ice dataset (Ludwig et al., 2020) and applied to the data. All observations and measurements with sea ice concentrations larger than 80 %, which is a typical choice for the definition of the sea ice edge, were excluded from further analysis. At this threshold value, sea ice still partially affects the measurements, but cloud formation begins as soon as small fractions of open ocean are present, and this initial phase should not be excluded from the analyses. Small variations of the threshold value did not significantly change the results. However, they showed more outliers in the measurements close to the sea ice edge or larger parts of the initial evolution of the clouds were excluded, respectively. Remaining issues due to the influence of the surface and misidentified sea ice apply only to measurements during the first minutes and kilometers above open ocean for the above-mentioned quantities. Measurements outside the marginal sea ice zone are not affected.

## 2.2 Backward trajectories

To study the evolution of cloud properties during the observed MCAOs in a quasi-Lagrangian framework, measurements and retrieval results were combined with backward airmass trajectories, which allow to assign every measurement the time or distance the airmass has traveled southwards since passing the sea ice edge. The backward trajectories were computed from ERA5 wind fields using Lagranto (Sprenger and Wernli, 2015). Every $1\,\mathrm{min}$ along each HALO flight track, a trajectory was initialized horizontally at the location of HALO, and vertically at $920\,\mathrm{hPa}$ pressure altitude, which roughly corresponds to cloud top. The trajectories were calculated backwards for 24 hours also tracing the sea ice concentration (SIC) from the combined AMSR2-MODIS dataset (Ludwig et al., 2020). The obtained backward trajectories have an improved reliability as the dropsondes released from the HALO aircraft have been assimilated in ERA5. The trajectories cover comparably short timescales and therefore the influence of errors remains small (Kirbus et al., 2024).

The time and distance, the airmass traveled above open ocean, was computed for every trajectory by integrating the fraction of open water (1 - SIC) over time and distance, similar to Spensberger and Spengler (2021). For better comparability, the evolution of the cloud properties is analyzed both as a function of time and distance above open ocean, as some studies use time while others use distance. In addition, the wind speed is not constant along the trajectories.

## 2.3 Overview of the research flights

During HALO–$(\mathcal{AC})^3$, MCAOs were sampled that evolved in different synoptic situations (Walbröl et al., 2024). Between 2022-03-21 and the end of the campaign on 2022-04-12, a long cold phase with several MCAOs occurred. Especially strong MCAO events, exceeding the 90th and 75th percentiles of the MCAO index climatology, were observed on 2022-03-25 and 2022-04-02, respectively (Walbröl et al., 2024). The strength of the MCAOs can be characterized through the MCAO index, which is defined as the difference of the potential skin temperature at the surface and the potential temperature at a pressure of $850\,\mathrm{hPa}$ (Fletcher et al., 2016)

$$M_{\text{CAO}} = \theta_{\text{skin}} - \theta_{\text{850hPa}}. \tag{1}$$

Larger differences are related to more intense MCAOs. MCAOs with indices indicating temperature differences between $0\,\mathrm{K} < M_{\text{CAO}} < 4\,\mathrm{K}$ are typically refered to as weak events, whereas MCAOs with $4\,\mathrm{K} < M_{\text{CAO}} < 8\,\mathrm{K}$ and $M_{\text{CAO}} > 8\,\mathrm{K}$ can be classified as moderate and strong events, respectively (Papritz and Spengler, 2017; Dahlke et al., 2022).

HALO conducted six flights during the cold phase of the campaign, which targeted MCAOs. An overview of the flights analyzed here is given in Fig. 1, where MODIS satellite images and the flight tracks and evaluated flight segments are shown for the research flights on 2022-03-21, 2022-03-28, 2022-03-29, 2022-03-30, 2022-04-01, and 2022-04-04. The research flights covered mostly the Fram Strait region, but for example on 2022-03-29 the area south-east of Svalbard was sampled. Some parts of the flights are affected by the topography of the island of Svalbard, causing, e.g., convergence lines downstream. The long cold period led to increasing sea ice extent north and south-east of Svalbard. The flight patterns mostly followed the quasi-Lagrangian sampling approach with flight legs oriented perpendicular to and along the wind direction (Wendisch

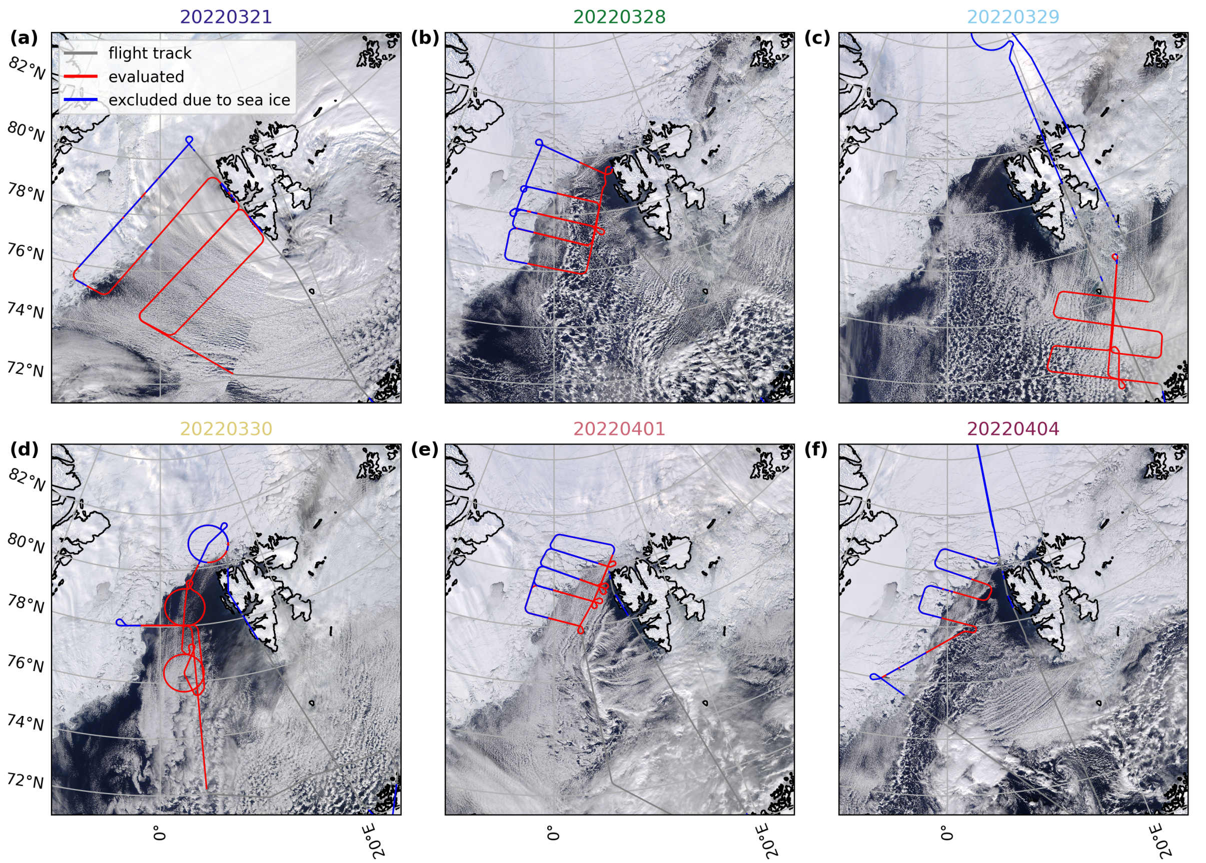


**Figure 1.** MODIS satellite images (Corrected Reflectance (True Color)) from NASA Worldview (https://worldview.earthdata.nasa.gov/) for all MCAO flights of HALO–$(\mathcal{AC})^3$. The ~~red~~ gray lines indicate the flight tracks, the red lines show the evaluated flight segments, and the blue lines are flight segments excluded due to sea ice.

et al., 2024). The strength of the observed MCAOs varied between the different research flights. The mean and maximum values of the MCAO index along the flight tracks of all research flights computed from ERA5 data (Hersbach et al., 2023a, b) are summarized in Table 1. The strongest observed MCAO events were on 2022-04-01 and on 2022-03-29. Weaker MCAO conditions were, for example, measured on 2022-03-30. In addition, the flights sampled different parts of the MCAOs. For example, the research flight on 2022-04-01 focused on the very initial phase of the MCAO, whereas the other research flights also covered regions further downstream. Thus, different parts of the temporal and spatial evolution were sampled.

The quasi-Lagrangian flight strategy applied to almost all flights of the HALO–$(\mathcal{AC})^3$ campaign (Wendisch et al., 2024) allows for studying the evolution of cloud properties during the observed MCAOs. Specifically, the temporal and spatial evolution of macroscopic cloud properties, such as the cloud top height, cloud fraction, and horizontal cloud extent, as well as

**Table 1.** Mean and maximum MCAO indices along flight track computed from ERA5 data (Hersbach et al., 2023a, b) for all MCAO flights of HALO–$(\mathcal{AC})^3$. The colors correspond to the colors of the research flights in Fig. 5 and 6.

| ~~Research~~ Date of research flight | Mean MCAO index [K] | Maximum MCAO index [K] |
|---|---|---|
| ~~20220321~~ 2022-03-21 | ~~1.91~~ 1.9 | ~~7.62~~ 7.6 |
| ~~20220328~~ 2022-03-28 | ~~3.28~~ 3.3 | ~~7.35~~ 7.4 |
| ~~20220329~~ 2022-03-29 | ~~5.32~~ 5.3 | ~~9.23~~ 9.2 |
| ~~20220330~~ 2022-03-30 | ~~0.44~~ 0.4 | ~~3.25~~ 3.3 |
| ~~20220401~~ 2022-04-01 | ~~6.59~~ 6.6 | ~~11.85~~ 11.9 |
| ~~20220404~~ 2022-04-04 | ~~1.89~~ 1.9 | ~~7.51~~ 7.5 |

the evolution of cloud microphysical properties, such as the effective radius of liquid water droplets and cloud thermodynamic phase partitioning, will be analyzed in the following.

## 3 Results

### 3.1 Case study: ~~MCAO~~ marine cold air outbreak observed on 2022-04-01

As a case study, the data collected on the research flight conducted by HALO on 2022-04-01 are analyzed first. The flight sampled the initial phase of a MCAO in the Fram Strait (see Fig. 1e). Average and maximum MCAO indices along the flight track of about 7 K and 12 K (see Table 1) classify this case as a moderate to strong event. ~~It~~ Based on the MCAO index, it appears as a typical event for the Fram Strait region during that time of the year ~~(Kirbus et al., 2024)~~(Walbröl et al., 2024; Kirbus et al., 2024). The satellite image in Fig. 1e shows cloud streets oriented along the mean wind direction from the sea ice edge towards the south to south-west. The event on 2022-04-01 was the strongest MCAO sampled during HALO–$(\mathcal{AC})^3$. In contrast to the other MCAO flights, the backward trajectories showed a clear northerly flow from the central Arctic towards the South without a significant influence of the topography of the island of Svalbard. In addition, collocated in situ measurements were collected on this day. Several studies have already analyzed data from the research flight on 2022-04-01. Kirbus et al. (2024) studied the thermodynamic evolution during this MCAO~~was studied by Kirbus et al. (2024)~~, based on dropsonde measurements during HALO–$(\mathcal{AC})^3$. In addition, Schirmacher et al. (2024) investigated the roll convection regime using radar observations. In the following, the temporal and spatial evolution of ~~the~~ macrophysical and microphysical cloud properties, including ~~the~~ cloud top height, cloud thermodynamic phase, and cloud droplet size, derived from passive remote sensing with specMACS will be presented and discussed. This complements existing studies about the MCAO observed on 2022-04-01 and contributes towards a complete picture of this case. The second part of this work (Weber et al., 2025a) additionally analyzes the vertical cloud structure observed on this day, exploiting the collocated remote sensing and in situ observations and building upon the results presented in the following.

### 3.1.1 Evolution of macrophysical cloud properties

First, the temporal and spatial evolution of the macrophysical cloud properties is analyzed for the flight on 2022-04-01. To this end, the cloud top height, the cloud fraction, and the cloud radius were derived from the specMACS measurements and combined with backward trajectories as described in Sect. 2.

Figure 2 shows the cloud top height (left column), cloud fraction (middle column), and cloud radius (right column) as a function of time (upper row) and distance (lower row) the airmass traveled above open ocean. The histograms for every time or distance bin are normalized by the total number of observations of the respective bin. In addition, Figure 3 displays RGB images taken by the polarization-resolving cameras at four points in time (about 30 min, 60 min, 90 min, and 150 min above open ocean) to illustrate the observed cloud morphology. Parts of Fig. 2 and 3 have also been shown in Wendisch et al. (2024).

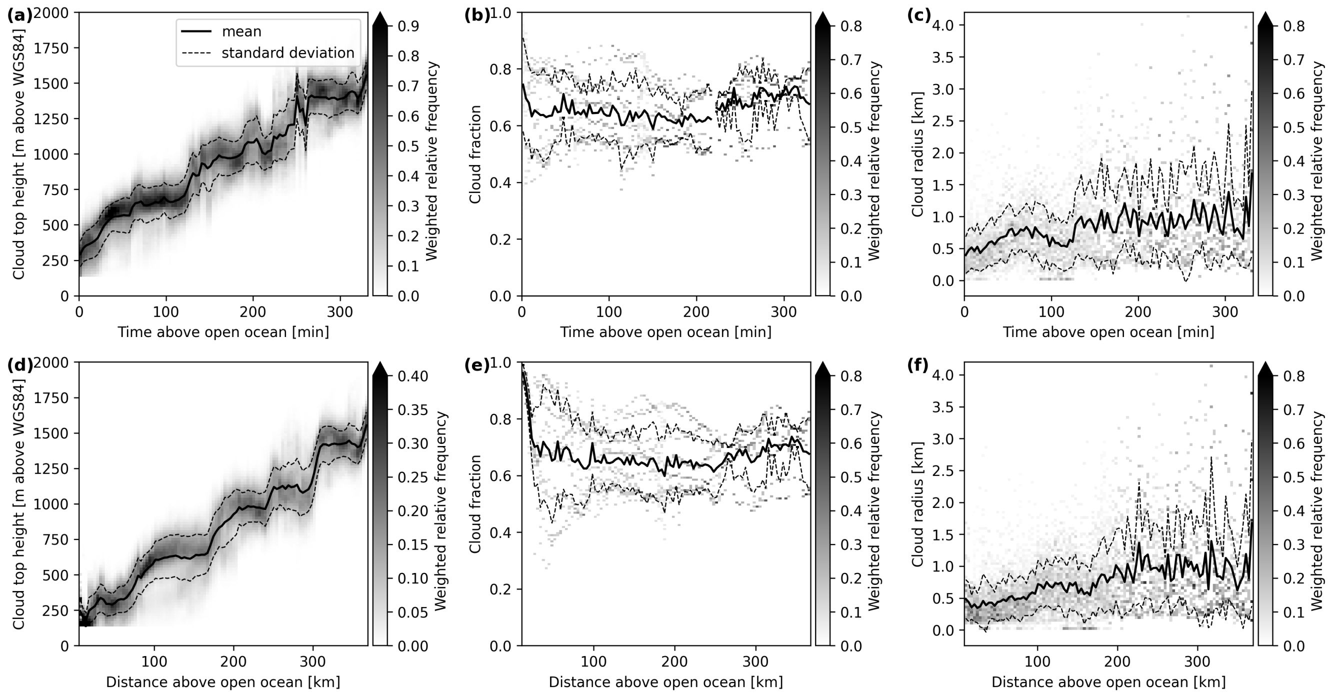


**Figure 2.** Histograms of cloud top height **(a, d)**, cloud fraction **(b, e)**, and cloud radius **(c, f)** as a function of time (upper row) and distance (lower row) above open ocean for the research flight on 2022-04-01. The solid black line indicates the mean and the dashed lines the standard deviation of the histograms. The cloud top heights are given above the World Geodetic System 1984 (WGS84) ellipsoid.

The cloud top height in Fig. 2a and 2d increases stepwise and almost linearly with time and distance from about 250 m close to the sea ice edge to about 1.5 km after 300 min. This increase ~~of~~ in cloud top height ~~with~~ over time is typical for the evolution of clouds during MCAOs, as the ABL deepens with time ~~(Murray-Watson et al., 2023; Kirbus et al., 2024). The~~ due to the strong surface heating (Brümmer, 1996; Murray-Watson et al., 2023; Kirbus et al., 2024). A similar increase in cloud top height from a few hundred meters to about 1 km during the first three hours above open ocean was also observed by

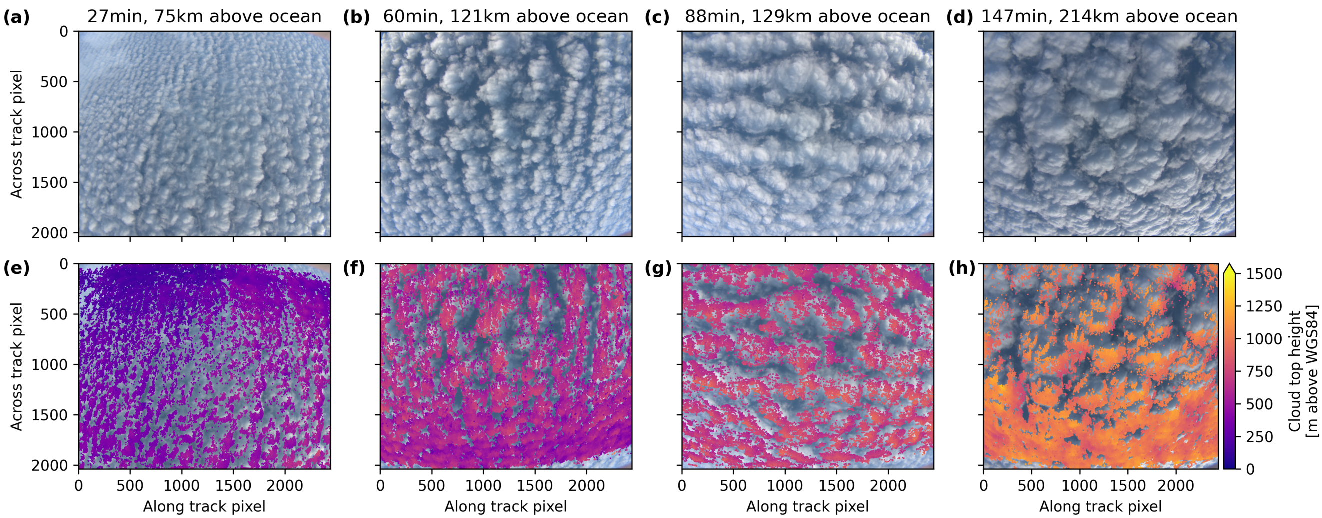


**Figure 3.** Example RGB images (upper row) and cloud top heights (lower row) at four different points in time, about 30 min, 60 min, 90 min, and 150 min above open ocean observed on 2022-04-01.

Schirmacher et al. (2024) derived from data measured by the radar installed on the Polar 5 aircraft operating on the same day in the same region.

The average cloud fraction (see Fig. 2b and 2e) remained almost constant during the first hours of the observed MCAO, as can also be seen in the RGB images in Fig. 3. ~~Cloud~~ The variability of the cloud fraction is high, showing values between 0.5 and 0.8, and is also almost constant with time. The cloud fractions close to unity ~~are observed at very small distances and times~~ during the first about 10 min and 10 km above open ocean ~~. These high cloud fractions~~ are due to the misidentification of bright sea ice in the marginal sea ice zone as clouds by the cloud mask ~~, which is based on the brightness. In contrast, Murray-Watson et al. (2023) found~~ and have to be considered as outliers, as discussed above. Schirmacher et al. (2024) observed a strong increase in the cloud cover during the first about 45 min followed by almost constant values for the MCAO on 2022-04-01 in the Fram Strait based on radar observations. This agrees with the specMACS observations, except for the initial increase, which is likely missed by the specMACS measurements due to the overestimation of the cloud fraction in the marginal sea ice zone. A statistical analysis of clouds during MCAOs by Murray-Watson et al. (2023), based on satellite observations, showed increasing cloud fractions during the first hours of MCAOs, followed by a slight decrease~~and generally slightly higher cloud fraction values. However, they used satellite observations with a much coarser spatial resolution of 25 compared to the high spatial resolution of 10 to 100 of the airborne specMACS observations, and the cloud fraction strongly depends~~. The almost constant cloud fraction observed on 2022-04-01 differs from this general statistical behavior. Based on the MCAO index, the MCAO on 2022-04-01 was typical for this region and time of the year (Walbröl et al., 2024). However, it is not necessarily representative for the average general statistics of MCAOs. The cloud streets and the mean wind direction on 2022-04-01 are not entirely perpendicular to the sea ice edge. The evolution of cloud properties downstream might therefore be influenced by fresh cold and dry air, which could, for example, explain deviations of the observed evolution of the cloud fraction on 2022-04-01 from the general statistics. Furthermore, the absolute values of the cloud fraction depend strongly on the threshold values applied in the cloud mask~~.~~, the sensitivities of the different instruments and their spatial resolutions, which can explain differences in absolute values across different studies. In addition, specMACS has a narrower field of view than satellite observations, which might affect the cloud fraction estimates.

Finally, the cloud radius increases from approximately 0.5 km to 1 km, with high variability. These results agree with the increasing roll circulation wavelength from initially 1 km to 2 km derived from ~~data measured by the radar installed on the Polar 5 aircraft on the~~ radar observations on the same day and in the same region (Schirmacher et al., 2024). The ~~cloud radius distribution~~ deepening of the ABL with increasing time above open ocean, driven by the strong surface heating, leads to increasing roll circulation wavelengths. This, in turn, affects the cloud field and could explain the increasing geometric size of the observed clouds with increasing time spent above open ocean (Brümmer, 1999). The cloud radius distribution generally consists of a mixture of smaller and larger clouds (see Fig. 3).

The different shapes of the curves describing, e.g., the evolution of the cloud top height during the first kilometers above open ocean compared to the first minutes above open ocean in Fig. 2 and similar figures in the following sections can be explained by changing wind speeds due to the off-ice acceleration at the sea ice edge ~~.~~ (Brümmer, 1996).

Moreover, the RGB images in Fig. 3 show cloud streets in panels (a) to (c), which are commonly observed in the initial phase of a MCAO (Brümmer, 1999). After about 150 min, more cellular structures evolve that are visible in panel (d), indicating a transition ~~of~~ in cloud morphology from ~~the cloud streets towards~~ cloud streets to a cellular cloud regime. The transition from rolls to cells is commonly explained by a decoupling of the ABL and accompanying precipitation formation (Brümmer, 1999; Gryschka and Raasch, 2005; McCoy et al., 2017; Abel et al., 2017; Pithan et al., 2018; Tornow et al., 2021). The decoupling of the ABL can be induced or reinforced by latent heat release due to condensation inside the clouds exceeding the surface heat fluxes, as well as by precipitation (Brümmer, 1999; Abel et al., 2017). Radar observations during the MCAO on 2022-04-01 indicate the presence of precipitation already after about one hour and show further increasing radar reflectivities with increasing time above open ocean (Schirmacher et al., 2024; Kirbus et al., 2024). In addition, surface heat fluxes derived from observations of this MCAO during HALO–$(\mathcal{AC})^3$ (Kirbus et al., 2024) show maxima during a similar time range as the transition of cloud morphology. A combination of measurements of thermodynamic, cloud, and dynamical properties could be used in the future to further investigate the reasons for the transition in cloud morphology observed during the MCAO on 2022-04-01.

#### 3.1.2 Cloud microphysical properties

The same analysis as for the macrophysical quantities was also performed for microphysical cloud characteristics such as the effective radius of liquid water droplets and the cloud thermodynamic phase, quantified through the ice index and ice fraction. Figure 4 displays the evolution of the effective radius of the liquid water droplets (a, d), the ice index (b, e), and the ice fraction (c, f) as a function of time and distance above open ocean. For later times (after approx. 210 min), no measurements of the effective radius and the ice fraction are available because the solar zenith angle during this part of the flight was too large for the cloudbow to be observed inside the field of view of the cameras, such that the retrievals could not be applied.

The effective radius of liquid cloud droplets shows a rapid increase from about $5\,\mu m$ to $7.5\,\mu m$ in the first approximately $30\,min$. It remains then constant until about $150\,min$ above open ocean, even though the cloud top height increases with time throughout the observed time period, which is usually accompanied by an increase in droplet size. At the same time, the ice index indicates the presence of ice crystals. Hence, the constant effective radius during this time could be explained by ice crystals competing with the supercooled liquid cloud droplets for the available water vapor, limiting the growth of liquid cloud droplets on the one hand, or freezing of larger cloud droplets on the other hand. The uncertainty of the measured effective radii of liquid cloud droplets from the cloudbow retrieval is smaller than the observed increase in the liquid cloud droplet size. Afterward, the effective radius becomes more variable and increases slightly, which coincides with the transition from cloud streets to cellular structures. In the more convective cellular regime, liquid water is formed in the convective updrafts at the centers of the cells, which could lead to further increasing effective radii at the higher cloud tops (Schirmacher et al., 2024; Maherndl et al., 2024). However, the number of measurements is also smaller in this time range due to larger solar zenith angles, and the results are therefore more uncertain. The spike in the evolution of the effective radius at ~~very small distances~~ distances smaller than $30\,km$ in panel (d) is due to the influence of sea ice, which was not completely filtered out and should be treated as an outlier. ~~The uncertainty of the measured effective radii of liquid cloud droplets from the cloudbow retrieval is $-0.2 \pm 1.6\,\mu m$, based on an evaluation with synthetic data (Volkmer et al., 2024; Pörtge, 2024). Therefore, the observed increase of the liquid cloud droplet size is outside the range of uncertainties.~~

~~The evolution of the effective radius of liquid cloud droplets during MCAOs was also studied by Murray-Watson et al. (2023), who found increasing effective radii with time and larger sizes between about $12\,\mu m$ and $18\,\mu m$. The effective radii were, however, derived from MODIS satellite data with a bispectral retrieval, which has large uncertainties for Arctic mixed-phase clouds and a much coarser spatial resolution. In addition, they focused on liquid water clouds only. In~~ In situ measurements of the effective radius conducted by the Polar 6 aircraft during the same day and in the same region show average effective radii of about $4\,\mu m$ during the first $100\,min$ above open ocean and slightly increasing radii for larger times (Moser et al., 2023). While the effective radii derived from cloudbow observations of specMACS are representative for the cloud top, the Polar 6 aircraft was flying lower inside the cloud. This could explain the slightly smaller observed values of the in situ measurements compared to the cloudbow retrieval results. The evolution of the effective radius of liquid cloud droplets during MCAOs was also studied by Murray-Watson et al. (2023), who also observed increasing effective radii with increasing time above open ocean.

The evolution of cloud thermodynamic phase is studied using the spectral ice index and the ice fractions from the polarized phase retrieval in the middle and right columns of Fig. 4, respectively. The results of the multi-angle polarimetric retrieval of the ice fraction and the spectral approach applied to derive the ice index have different penetration depths. Both are representative for the cloud top, but the spectral signal originates from slightly deeper altitudes within the cloud than the polarized signal~~.~~, as discussed in Sect. 2.1. The ice index is smaller than 20 during the first $30\,min$, indicating a pure liquid water cloud. Subsequently, it transforms into a mixed-phase cloud with slightly increasing ice indices over time. The transition from pure liquid water to the mixed phase occurs during the same time range as the rapid increase of the effective radius at the beginning.

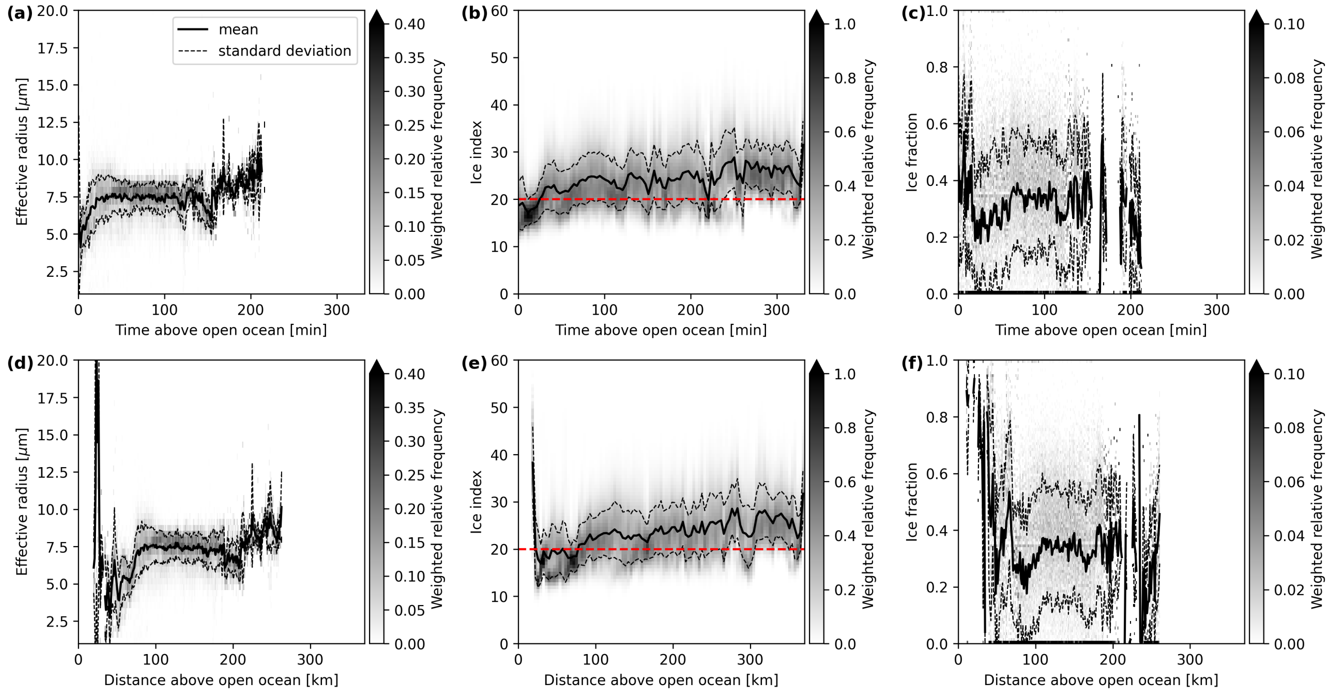


**Figure 4.** Histograms of the effective radius of the liquid water droplets **(a, d)**, the ice index **(b, e)**, and the ice fraction **(c, f)** as a function of time (upper row) and distance (lower row) above open ocean for the research flight on 2022-04-01. The black solid line indicates the mean ~~,~~ and the black dashed line the standard deviation of the histograms. The red dashed line in panels **(b)** and **(e)** is the threshold value between the liquid water and the mixed phase.

Larger effective radii increase the probability for freezing of liquid water droplets and heterogeneous ice formation. In addition, during the same time range, the cloud top height increased and the cloud top temperature decreased. Thus, a threshold temperature and size of the cloud liquid water droplets could be reached that initiate the formation of ice crystals.

The evolution of the ice fraction shows a similar structure. The higher ice fractions during the first 25 min and 50 km close to the sea ice edge are caused by a misclassification of sea ice as cloud~~. The cloud mask using the spectral data is more accurate here, as a wavelength of 1640 is applied, where sea ice is comparably dark. The cloud mask for the polarized retrieval is more affected by sea ice. Considering the~~ , as discussed above. Considering these initially high ice ~~fraction~~ fractions as outliers and taking the bias of the ice fraction for the cloudbow range into account (Weber et al., 2025b), the ice fraction at the beginning was in the range of 0.2. It then increases until about 90 min above open ocean and ~~stays almost constant~~ remains almost constant afterwards, but the cloud top is still dominated by liquid water. The initially faster decrease of the ice fraction appears slightly later than the increase of the spectral ice index, which is more sensitive to ice and representative for slightly lower altitudes, deeper within the cloud~~.~~ , but still at cloud top. Ice crystals forming at the cloud top and sedimenting downward might first increase the relative amount of ice at slightly lower altitudes if the sedimentation speed is faster than the ice formation. Further discussions of the vertical cloud structure can be found in the second part of this work in Weber et al. (2025a). From around 150 min above open ocean, when the transition from cloud streets to cells was observed, the ice fraction becomes variable but also uncertain.

### 3.2 Statistics of all ~~six MCAOs~~observed marine cold air outbreaks

After studying the temporal and spatial evolution of cloud macrophysical and microphysical properties during the MCAO on 2022-04-01, the analyses are extended to all research flights targeting MCAOs. The different observed MCAOs cover a variety of different conditions, as discussed in Sect. 2.3. This allows to further investigate the variability of the cloud evolution between different events and the dependence on the strength of the MCAO.

#### 3.2.1 Evolution of macrophysical cloud properties

Similar to above, the temporal and spatial evolution of the macrophysical cloud properties is analyzed first. To this end, the cloud top height, the cloud fraction, and the cloud radius were derived from the specMACS measurements and combined with backward trajectories as described in Sect. 2 for all research flights. Figure 5 displays histograms of these quantities as a function of time (upper row) and distance (lower row) above open ocean together with their mean for all flights in different colors. The first, second, and third columns correspond to the cloud top height, cloud fraction, and cloud radius, respectively. In general, there is a large variability between the different research flights, which were performed under varying MCAO conditions and partly in different regions.

The cloud top height in panels (a) and (d) increases with time and distance from the ~~ice edge for all research flights~~ sea ice edge from a few hundred meters to a maximum of about 2.5 km~~.~~, depending on the research flight. Increasing cloud top heights with time are expected as the boundary layer generally deepens with time during a MCAO. The largest cloud top heights are observed during the flights on 2022-04-01 (purple line) and 2022-03-29 (green line), which were the strongest observed MCAOs, and lower cloud top heights are reached during the weaker MCAOs. In addition, the increase is faster for these strong events compared to the weaker ones. Larger cloud top heights for stronger MCAOs were also observed by Murray-Watson et al. (2023) and Schirmacher et al. (2024). This can be expected as stronger temperature differences lead to larger surface heat fluxes, increased instability, deeper ABLs, and therefore larger cloud top heights. The very large cloud top heights on 2022-03-21 at large times and distances between 1100 and 1200 min and 900 to 1000 km above open ocean are due to high-level cirrus clouds south-west of Svalbard, as can also be seen in Fig. 1a.

A similar picture is found for the horizontal cloud extent in Fig. 5c and 5f. The cloud radius generally increases with time and distance above open ocean from a few hundred meters to about 1.5 km. Larger cloud radii are associated with the stronger events on 2022-04-01 and 2022-03-29, and smaller radii are observed during the weaker events on 2022-04-04, 2022-03-30, and 2022-03-28. Similar to the cloud top height, the increase of the cloud radius is faster for stronger events than for weaker MCAOs. Larger cloud top heights can be related to larger ABL heights and therefore larger roll circulations, which affect the cloud field (Brümmer, 1999), and could explain the observed horizontal cloud extents.

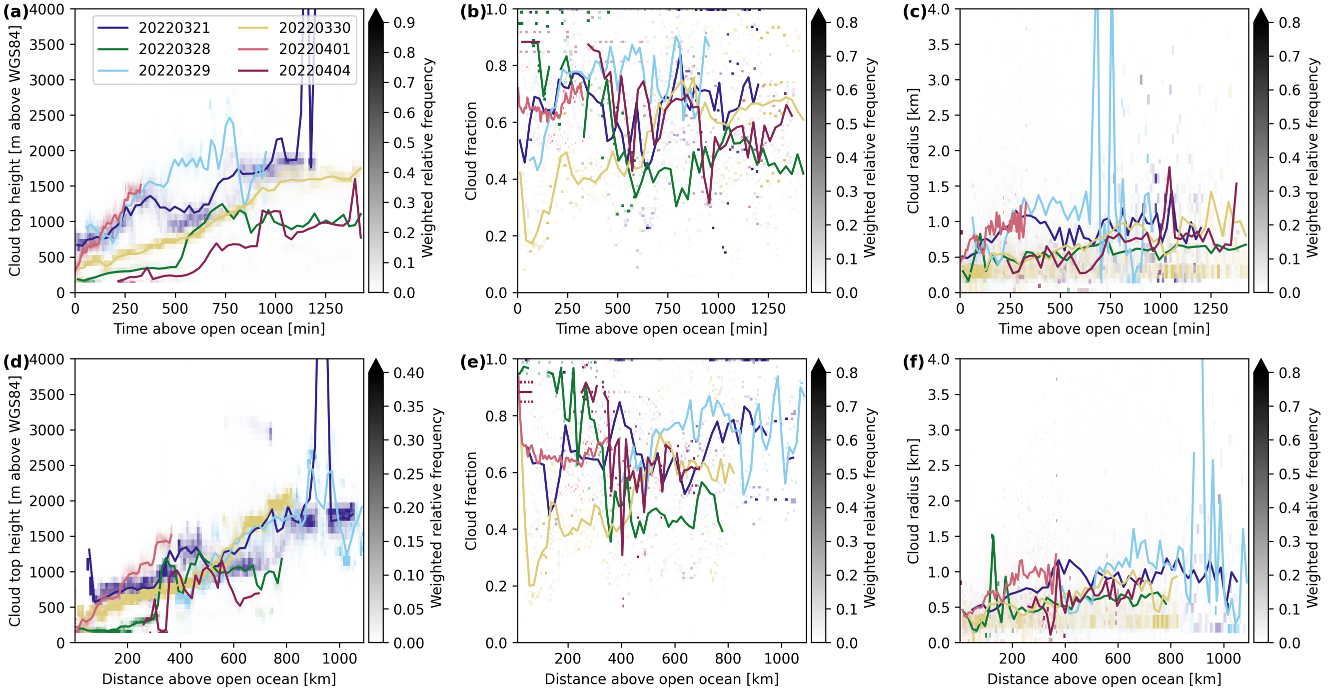


**Figure 5.** Histograms of cloud top height **(a, d)**, cloud fraction **(b, e)**, and cloud radius **(c, f)** as a function of time (upper row) and distance (lower row) above open ocean with their respective mean for all MCAO flights during HALO–$(\mathcal{AC})^3$. The different colors correspond to the different research flights and the solid lines denote the respective means.

In contrast, the cloud fraction shows a more ~~complicated~~ complex behavior and a large variability. ~~Cloud fractions close to 1 are observed at very small distances and times above open ocean. These high cloud fractions are due to the misidentification of bright sea ice~~ In addition to the possible overestimation of the cloud fraction in the marginal ~~ice zone as clouds by the cloud mask, as discussed above. In addition,~~ sea ice zone, there are some island effects ~~affecting~~ visible, affecting the cloud cover (see Fig. 1). In general, the cloud fraction remains either relatively constant or increases with time, with typical values between 0.4 and 0.8. The stronger MCAOs in Fig. 5 tend to have larger cloud fractions compared to the weaker ones. This agrees with the observations of larger cloud fractions during the first hours of MCAOs for stronger events by Murray-Watson et al. (2023). The flight on 2022-03-28 is an exception and strongly affected by the local topography of Svalbard.

#### 3.2.2 Evolution of microphysical cloud properties

Similar to the macrophysical cloud properties, the temporal and spatial evolution of cloud microphysical properties and their variability and dependence on the MCAO strength are investigated by combining measurements with backward trajectories, as in the previous sections. Figure 6 displays the effective radius of liquid cloud droplets, the ice index, and the ice fraction in the first, second, and third column, respectively, as a function of time (upper row) and distance (lower row) above open ocean.

The effective radius of liquid cloud droplets increases with time and distance above open ocean, and sizes between about 3 µm and 17 µm were observed. Larger effective radii are reached during the stronger events on 2022-04-01 and 2022-03-29, for which the growth of the cloud droplets is also faster. This can be expected as the effective radius in general increases with height within a cloud, and larger cloud top heights were observed for stronger MCAOs in Fig. 5. ~~In contrast,~~ The MCAOs observed on 2022-03-21 and 2022-03-28 had, however, similar strengths, but very different cloud droplet effective radii were observed. A reason for this could be differences in the aerosol conditions, since the aerosol concentration generally strongly affects the cloud droplet number concentration and the droplet size.

Murray-Watson et al. (2023) found also increasing effective radii with time, but smaller effective radii ~~for~~ during the initial phase of stronger MCAOs compared to weaker events~~. However, they focused on liquid-dominated clouds only~~, and, in general, larger droplet sizes between about 12 µm and ~~the retrieved effective radii from satellite observations are much more uncertain and have a much coarser spatial resolution than the effective radii derived with the polarimetric cloudbow retrieval.~~ 18 µm. There are several possible reasons for these differences. The effective radii in Murray-Watson et al. (2023) were derived from MODIS satellite data with a bispectral retrieval, whereas the effective radii in this work were obtained from the polarimetric cloudbow retrieval. Both retrievals have different sensitivities, penetration depths, and spatial resolutions, which can lead to differences in the derived absolute values of the effective radii. In addition, Murray-Watson et al. (2023) focused on liquid water clouds only, while in this work mixed-phase clouds were also included in the analyses. The presence of ice crystals can lead to smaller cloud droplet sizes, since liquid water and ice in mixed-phase clouds compete for the available water vapor and larger cloud droplets are more likely to freeze. This, together, could explain the differences in the absolute values of the observed cloud droplet radii. The differences in the effective radii between stronger and weaker events could, for example, be related to differences in the aerosol conditions. Murray-Watson et al. (2023) observed large differences in the evolution of the liquid water path and cloud droplet number concentration between weak and strong MCAOs with high and low aerosol conditions. During HALO–$(\mathcal{AC})^3$ only a limited number of six MCAOs were observed, which show a large variability. Nevertheless, they might not be entirely representative for the general statistics of strong and weak MCAOs. The observed MCAOs occurred in different regions, were partly affected by the topography of Svalbard, and differed in synoptic conditions and airmass history across the six events. A larger number of samples would be required for more robust statistics, but the six cases already provide valuable insights into the temporal and spatial cloud evolution and its variability during MCAOs.

~~Concerning~~

Regarding the cloud thermodynamic phase, the ice indices and ice fractions generally increase with time above open ocean. The patterns of both ice index and ice fraction are very similar. Initial values of the ice index are below or around 20, which is the threshold value between liquid water and mixed-phase clouds, and increase to about 30 to 50, depending on the research flight. In addition, the ice fraction increases with time and distance from very small values around 0.2 to approximately 0.5 to 0.8. The ice fraction is overestimated at very small times and distances below 100 min and 100 km above open ocean close to the sea ice edge due to the misclassification of sea ice in the marginal sea ice zone as clouds. The large variability of both the ice index and ice fraction also reflects the larger uncertainty in the thermodynamic phase retrievals compared to the stereographic or the cloudbow retrieval. The described increase in the ice index and ice fraction indicates a transition from a liquid water to a

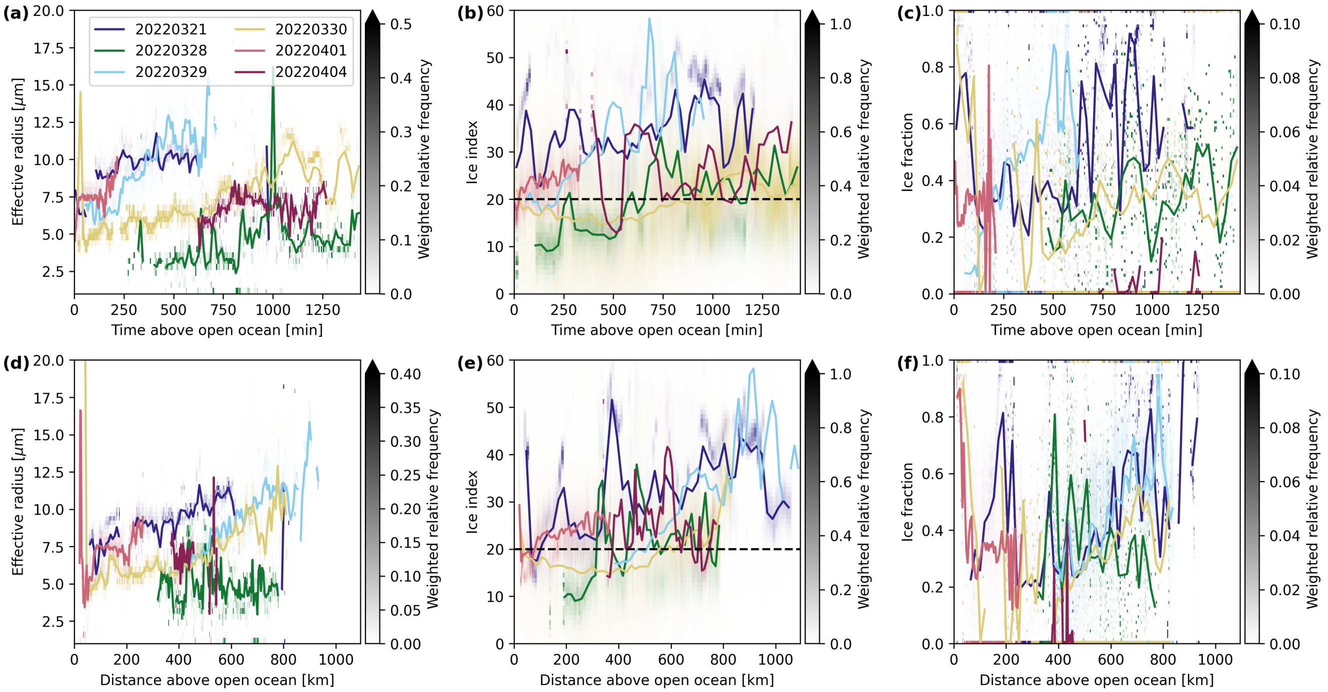


**Figure 6.** Histograms of effective radius of liquid cloud droplets **(a, d)**, ice index **(b, e)**, and ice fraction **(c, f)** as a function of time (upper row) and distance (lower row) above open ocean for all MCAO flights of HALO–$(\mathcal{AC})^3$, The solid lines indicate the mean of the respective flight, the black dashed line in panels **(b)** and **(e)** is the threshold value between the liquid water and the mixed phase.

mixed-phase regime with increasing amounts of ice. This phase transition is faster for the stronger observed MCAOs on 2022-04-01, 2022-03-29, and 2022-03-21. In addition, stronger events reach higher ice indices and ice fractions. The faster phase transition and higher ice fractions for stronger events agree with the higher observed cloud top heights and larger effective radii for these events, since typically colder temperatures at higher altitudes and larger cloud droplets increase the probability of ice formation, which typically happens through heterogeneous freezing (de Boer et al., 2011; Cui et al., 2006; Ansmann et al., 2005). Similar to the case study of the MCAO on 2022-04-01, the phase transition coincides with an increase ~~of~~ in the effective radius of the liquid cloud droplets and increasing cloud top heights during all observed cases. This indicates that a threshold cloud top height respectively cloud top temperature and cloud droplet size are reached, initiating ice formation.

## 4 Summary and conclusions

In this work, the spatial and temporal evolution of macrophysical and microphysical cloud properties during the initial phase of marine cold air outbreaks in the Arctic was studied with a focus on cloud thermodynamic phase partitioning and phase transitions. To this end, quasi-Lagrangian airborne passive remote sensing observations collected with specMACS during the HALO–$(\mathcal{AC})^3$ campaign in the Arctic were combined with backward airmass trajectories. The evolution of cloud macrophysical and microphysical properties was analyzed for all ~~flights targeting MCAOs~~ six flights targeting marine cold air outbreaks (MCAOs) and compared to investigate also the variability of the cloud evolution and the dependence on the MCAO strength. The presented analyses use high-resolution, quasi-Lagrangian airborne observations of the evolution of clouds during MCAOs, complementing existing studies based on coarser resolved satellite observations. In addition, the evolution of the cloud thermodynamic phase partitioning and phase transitions were studied, which have not been investigated previously in a quasi-Lagrangian framework. Multi-angle polarimetric observations allow for the derivation of a quantitative ice fraction, which, in combination with the qualitative ice index based on spectral measurements, provides information about the cloud thermodynamic phase at two different altitudes close to cloud top.

A case study of a strong MCAO observed on 2022-04-01 in the Fram Strait showed increasing cloud top heights and horizontal cloud extents with increasing time and distance above open, sea ice-free ocean, while the cloud fraction stayed almost constant during the observed first five hours of the MCAO. Moreover, the effective radius of liquid water droplets increased from about 5 µm to 7.5 µm during the first approximately 30 min and remained constant afterward. ~~This~~ The initial increase of the effective radius coincided with an increase ~~of~~ in the ice index and ice fraction and a transition from a pure liquid water to a mixed-phase cloud regime. This indicated that a threshold cloud top temperature and droplet size for ice formation in the observed clouds might have been reached.

The same analysis was repeated for all six observed MCAOs. The cloud top heights and horizontal extents increased with time and distance traveled above open ocean during all MCAOs. However, the increase was stronger and faster for more intense MCAOs. Similarly, the effective radius of liquid cloud droplets increased over time and reached larger sizes for stronger MCAOs. Furthermore, increasing ice indices and ice fractions with time and a transition from an initially liquid water to a mixed-phase regime were observed during all MCAOs. This transition happened earlier for stronger MCAO, and larger ice indices and ice fractions were reached for the stronger events. In all observed cases, the transition from the liquid water to the mixed phase coincided with an increase of the effective radius of the liquid cloud droplets and the cloud top height. As the ABL and clouds evolve and the cloud top height increases, the liquid cloud droplets grow to larger sizes and the cloud top temperature typically decreases, leading to an increasing probability of ice formation through heterogeneous freezing. In general, a large variability was observed between the different MCAO cases measured during HALO–$(\mathcal{AC})^3$. The measurements were performed in partly different regions, with different MCAO strengths, different parts of the evolution were sampled, and some island effects also affected the measurements. Only a small number of six MCAO could be studied, which, however, covered a large range of MCAO conditions (Walbröl et al., 2024).

Some limitations of the presented results should be considered. The brightness-based cloud mask for the polarization-resolving cameras of specMACS struggles in the presence of sea ice, where ice can falsely be identified as clouds. This is a known issue for cloud masks based on passive imaging methods. ~~Thus, an~~ A sea ice mask was applied to consider measurements above open ocean only and to filter the most uncertain results. However, some artifacts in the marginal sea ice zone remained, which were treated as outliers. An improved cloud mask ~~should~~ could be developed in the future to improve the results of the analyses and avoid outliers in the measurements in the marginal ice zone during the very initial phase of the cloud evolution. In addition, the large solar zenith angles in the Arctic lead to increased uncertainties of the retrievals of the specMACS instrument.

On the one hand, three-dimensional radiative effects have a stronger influence on the phase retrievals for large solar zenith angles. On the other hand, the cloudbow retrieval used for the retrievals of the droplet size and ice fraction is then observed at the edge of the field of view of the polarization-resolving cameras, where the measurement uncertainties are larger (Weber et al., 2024). The results of the cloudbow retrieval and the polarized phase partitioning retrieval were filtered, excluding~~for example~~ , for example, retrieval results with a large root mean square error between the fitted model and the measurement ~~,~~ to eliminate the most uncertain results.

Furthermore, it should be mentioned that the definition of the ice fraction varies strongly between different studies, depending on the type of measurements and the application (Korolev et al., 2017). In addition, different threshold values are used to define the liquid water, mixed, and ice ~~phase~~phases. This must be kept in mind when comparing the results of different studies on phase partitioning. In this work, the ice fraction is an optical ice fraction defined by the optical thickness, and the ice index is a qualitative measure of cloud thermodynamic phase.

~~The quasi-Lagrangian airborne measurements applied in this work complement satellite-based studies as they have a much higher spatial resolution and additional cloud properties, such as cloud thermodynamic phase partitioning, can be studied. The~~ The observations of the temporal and spatial evolution of cloud macrophysical and micropyhsical properties during the initial phase of MCAOs presented in this work provide unique observational data, which could be used for model evaluation in ~~the future~~ future work. Mixed-phase clouds, their thermodynamic phase partitioning ~~, and their~~ and evolution during meridional airmass transformations, such as MCAOs, are not well represented in models. The presented observations could be compared to model results in a Eulerian and a quasi-Lagrangian way for the six observed MCAOs, similar to Wendisch et al. (2025) who analyzed the thermodynamic evolution of MCAOs in dropsonde observations and in the ICON weather prediction model. ~~Furthermore, based on the analyses of the temporal and spatial evolution of clouds during MCAOs during HALO–$(\mathcal{AC})^3$, the vertical cloud structure and its evolution during a MCAO is investigated in the second part of this work in Weber et al. (2025a)~~ The macrophysical cloud properties, such as the cloud top height, can be directly derived from typical model output and be compared to measurements. In addition, the ice fraction and effective radius of liquid cloud droplets can be computed from model output as described in Volkmer et al. (2024) and Weber et al. (2025b). A forward operator is only needed for a direct comparison of modeled and measured ice indices, as the ice index is a qualitative measure of the cloud thermodynamic phase and computed from measured radiances.

In the analyses presented in this work, the MCAOs were distinguished in terms of their strength, quantified through the MCAO index. Besides the MCAO intensity, the aerosol concentration also affects the evolution of cloud properties (Murray-Watson et al., 2023) and was not considered so far. The effect of aerosols on the cloud properties could be further studied in the future, using, for example, collocated in situ measurements and lidar observations on board HALO during HALO–$(\mathcal{AC})^3$ to characterize the aerosol conditions.

Furthermore, based on the analyses of the temporal and spatial evolution of clouds during MCAOs during HALO–$(\mathcal{AC})^3$, the vertical cloud structure and its evolution during a MCAO is investigated in the second part of this work in Weber et al. (2025a) . Weber et al. (2025a) also includes a comparison to active remote sensing observations and additionally applies collocated in situ observations.

*Code and data availability.* The data collected during the HALO–$(\mathcal{AC})^3$ campaign are published on PANGAEA (Ehrlich et al., 2025). The measurements of the SWIR camera of specMACS are available at Weber et al. (2024). Retrieval results from specMACS, the HALO backward trajectories, and the analysis codes used in this work can be provided upon request from the corresponding author.

## Appendix A: Retrieval of horizontal cloud extent

In the following, the retrieval of horizontal cloud extent from measurements of specMACS will be described in more detail. The content of this section has already been published in Weber (2025). To determine the horizontal extent of clouds in two-dimensional images, clouds must be identified and clustered. From the measurements from the polarization-resolving cameras, the 3D cloud geometry can be reconstructed using the stereographic retrieval method of Kölling et al. (2019). These data can be applied in a watershedding algorithm similarly to topographic data to cluster individual clouds. Here, the watershedding algorithm implemented in the Tracking and Object-Based Analysis of Clouds (TOBAC) package (Heikenfeld et al., 2019; Sokolowsky et al , which is specifically designed for cloud identification and tracking in meteorological applications, was used. Fig. A1a displays the derived cloud top heights for one flight segment observed on 2022-04-01. In the cloud size retrieval, features are first detected as extreme values above several subsequent threshold heights between the minimum and maximum cloud top height of a flight segment. The identified features are highlighted as crosses in Fig. A1. Next, the segmentation is performed. The difficulty here is to determine the threshold heights for the watershedding since the cloud height varied significantly during a research flight during HALO–$(\mathcal{AC})^3$ as the clouds and ABL evolved with time and distance from the sea ice edge. This is also visible in the example segment in Fig. A1a, where the cloud top height differs between the beginning (upper left) with lower heights closer to the ice edge and the end (lower right, larger heights) of the segment. Thus, an adaptive threshold based on the average cloud top height over a small time interval was defined. A threshold height of 200 m below the average cloud top height, with a minimum of 100 m and a maximum of 500 m, was chosen after trying different settings. Figure A1b shows the resulting segmentation with the different cloud clusters color-coded. Finally, TOBAC provides the geometric areas of the clusters from which cloud radii were computed, assuming circular shapes. The threshold values were tuned such that the algorithm provided reasonable cloud clusters, as displayed in Fig. A1b, during both the initial phase and later during the cloud evolution. Depending on the choice of the threshold values for the feature detection and segmentation, larger or smaller cloud sizes were obtained, but this applied to the entire temporal evolution of the clouds.

*Author contributions.* AW evaluated all data, performed the analyses, and wrote the manuscript with input from all co-athours. BK computed the backward trajectories. MW and BM provided valuable feedback to the analyses and the outline of the study. All authors contributed to the discussion of the results.

*Competing interests.* The authors declare that they have no conflict of interest.

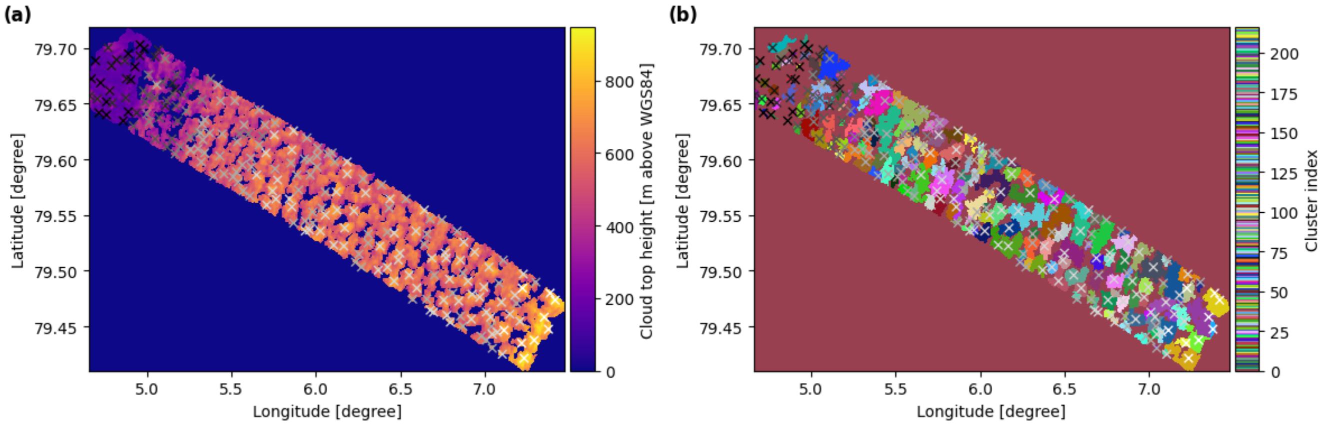


**Figure A1.** (a) Cloud top height of the cloud targets for a flight segment measured on 2022-04-01. (b) Identified features and segmented cloud clusters. The crosses indicate the detected features, and the colors display the results of the segmentation. This figure has already been published in Weber (2025).

*Acknowledgements.* We would like to thank Fabian Hoffmann for valuable discussions about cloud microphysics. In addition, we thank Lea Volkmer for applying the stereographic retrieval to the specMACS observations and thank the entire HALO–$(\mathcal{AC})^3$ team involved in the realization of the measurement flights and the data processing. Furthermore, we thank the Institute of Environmental Physics, University of Bremen for the provision of the merged MODIS-AMSR2 sea-ice concentration data at https://data.seaice.uni-bremen.de/modis_amsr2 (last access 2023-09-18). We are further grateful for funding of project grant no. 316646266 and 442667104 by the Deutsche Forschungsgemeinschaft (DFG, German Research Foundation) within the framework of Priority Programme SPP 1294 to promote research with HALO. ~~Furthermore~~In addition, we appreciate the funding provided by DFG – Project-ID 268020496 – TRR 172.

## References


Abel, S. J., Boutle, I. A., Waite, K., Fox, S., Brown, P. R. A., Cotton, R., Lloyd, G., Choularton, T. W., and Bower, K. N.: The Role of Precipitation in Controlling the Transition from Stratocumulus to Cumulus Clouds in a Northern Hemisphere Cold-Air Outbreak, Journal of the Atmospheric Sciences, 74, 2293 – 2314, https://doi.org/10.1175/JAS-D-16-0362.1, 2017.

Ahn, E., Huang, Y., Siems, S. T., and Manton, M. J.: A Comparison of Cloud Microphysical Properties Derived From MODIS and CALIPSO With In Situ Measurements Over the Wintertime Southern Ocean, Journal of Geophysical Research: Atmospheres, 123, 11,120–11,140, https://doi.org/10.1029/2018JD028535, 2018.

Ansmann, A., Mattis, I., Müller, D., Wandinger, U., Radlach, M., Althausen, D., and Damoah, R.: Ice formation in Saharan dust over central Europe observed with temperature/humidity/aerosol Raman lidar, J. Geophys. Res., 110, https://doi.org/10.1029/2004JD005000, 2005.

Block, K., Schneider, F. A., Mülmenstädt, J., Salzmann, M., and Quaas, J.: Climate models disagree on the sign of total radiative feedback in the Arctic, Tellus A: Dynamic Meteorology and Oceanography, 2020.

Boettcher, M., Schäfler, A., Sprenger, M., Sodemann, H., Kaufmann, S., Voigt, C., Schlager, H., Summa, D., Di Girolamo, P., Nerini, D., Germann, U., and Wernli, H.: Lagrangian matches between observations from aircraft, lidar and radar in a warm conveyor belt crossing orography, Atmospheric Chemistry and Physics, 21, 5477–5498, https://doi.org/10.5194/acp-21-5477-2021, 2021.

Brümmer, B.: Boundary-layer modification in wintertime cold-air outbreaks from the Arctic sea ice, Boundary-Layer Meteorology, 80, 109–125, https://doi.org/10.1007/BF00119014, 1996.

Brümmer, B.: Roll and Cell Convection in Wintertime Arctic Cold-Air Outbreaks, Journal of the Atmospheric Sciences, 56, 2613 – 2636, https://doi.org/10.1175/1520-0469(1999)056<2613:RACCIW>2.0.CO;2, 1999.

Cesana, G., Waliser, D. E., Jiang, X., and Li, J.-L. F.: Multimodel evaluation of cloud phase transition using satellite and reanalysis data, Journal of Geophysical Research: Atmospheres, 120, 7871–7892, https://doi.org/10.1002/2014JD022932, 2015.

Cesana, G. V., Khadir, T., Chepfer, H., and Chiriaco, M.: Southern Ocean Solar Reflection Biases in CMIP6 Models Linked to Cloud Phase and Vertical Structure Representations, Geophysical Research Letters, 49, e2022GL099 777, https://doi.org/10.1029/2022GL099777, e2022GL099777 2022GL099777, 2022.

Choi, Y.-S., Ho, C.-H., Park, C.-E., Storelvmo, T., and Tan, I.: Influence of cloud phase composition on climate feedbacks, Journal of Geophysical Research: Atmospheres, 119, 3687–3700, https://doi.org/10.1002/2013JD020582, 2014.

Cohen, J., Zhang, X., Francis, J., Jung, T., Kwok, R., Overland, J., Ballinger, T. J., Bhatt, U. S., Chen, H. W., Coumou, D., Feldstein, S., Gu, H., Handorf, D., Henderson, G., Ionita, M., Kretschmer, M., Laliberte, F., Lee, S., Linderholm, H. W., Maslowski, W., Peings, Y., Pfeiffer, K., Rigor, I., Semmler, T., Stroeve, J., Taylor, P. C., Vavrus, S., Vihma, T., Wang, S., Wendisch, M., Wu, Y., and Yoon, J.: Divergent consensuses on Arctic amplification influence on midlatitude severe winter weather, Nature Climate Change, 10, 20–29, https://doi.org/10.1038/s41558-019-0662-y, 2020.

Cui, Z., Carslaw, K. S., Yin, Y., and Davies, S.: A numerical study of aerosol effects on the dynamics and microphysics of a deep convective cloud in a continental environment, Journal of Geophysical Research: Atmospheres, 111, https://doi.org/10.1029/2005JD005981, 2006.

Dahlke, S., Solbès, A., and Maturilli, M.: Cold Air Outbreaks in Fram Strait: Climatology, Trends, and Observations During an Extreme Season in 2020, Journal of Geophysical Research: Atmospheres, 127, e2021JD035 741, https://doi.org/10.1029/2021JD035741, e2021JD035741 2021JD035741, 2022.

de Boer, G., Morrison, H., Shupe, M. D., and Hildner, R.: Evidence of liquid dependent ice nucleation in high-latitude stratiform clouds from surface remote sensors, Geophysical Research Letters, 38, https://doi.org/10.1029/2010GL046016, 2011.

Ehrlich, A., Bierwirth, E., Wendisch, M., Gayet, J.-F., Mioche, G., Lampert, A., and Heintzenberg, J.: Cloud phase identification of Arctic boundary-layer clouds from airborne spectral reflection measurements: test of three approaches, Atmospheric Chemistry and Physics, 8, 7493–7505, https://doi.org/10.5194/acp-8-7493-2008, 2008.

Ehrlich, A., Wendisch, M., Bierwirth, E., Gayet, J.-F., Mioche, G., Lampert, A., and Mayer, B.: Evidence of ice crystals at cloud top of Arctic boundary-layer mixed-phase clouds derived from airborne remote sensing, Atmospheric Chemistry and Physics, 9, 9401–9416, https://doi.org/10.5194/acp-9-9401-2009, 2009.

Ehrlich, A., Crewell, S., Herber, A., Klingebiel, M., Lüpkes, C., Mech, M., Becker, S., Borrmann, S., Bozem, H., Buschmann, M., Clemen, H.-C., De La Torre Castro, E., Dorff, H., Dupuy, R., Eppers, O., Ewald, F., George, G., Giez, A., Grawe, S., Gourbeyre, C., Hartmann, J., Jäkel, E., Joppe, P., Jourdan, O., Jurányi, Z., Kirbus, B., Lucke, J., Luebke, A. E., Maahn, M., Maherndl, N., Mallaun, C., Mayer, J., Mertes, S., Mioche, G., Moser, M., Müller, H., Pörtge, V., Risse, N., Roberts, G., Rosenburg, S., Röttenbacher, J., Schäfer, M., Schaefer, J., Schäfler, A., Schirmacher, I., Schneider, J., Schnitt, S., Stratmann, F., Tatzelt, C., Voigt, C., Walbröl, A., Weber, A., Wetzel, B., Wirth, M., and Wendisch, M.: A comprehensive in situ and remote sensing data set collected during the HALO–$(\mathcal{AC})^3$ aircraft campaign, Earth System Science Data, 17, 1295–1328, https://doi.org/10.5194/essd-17-1295-2025, 2025.

Ewald, F., Kölling, T., Baumgartner, A., Zinner, T., and Mayer, B.: Design and characterization of specMACS, a multipurpose hyperspectral cloud and sky imager, Atmospheric Measurement Techniques, 9, 2015–2042, https://doi.org/10.5194/amt-9-2015-2016, 2016.

Field, P. R., Cotton, R. J., McBeath, K., Lock, A. P., Webster, S., and Allan, R. P.: Improving a convection-permitting model simulation of a cold air outbreak, Quarterly Journal of the Royal Meteorological Society, 140, 124–138, https://doi.org/10.1002/qj.2116, 2014.

Field, P. R., Brozkova, R., Chen, M., Dudhia, J., Lac, C., Hara, T., Honnert, R., Olson, J., Siebesma, P., de Roode, S., Tomassini, L., Hill, A., and McTaggart-Cowan, R.: Exploring the convective grey zone with regional simulations of a cold air outbreak, Quarterly Journal of the Royal Meteorological Society, 143, 2537–2555, https://doi.org/10.1002/qj.3105, 2017.

Fletcher, J., Mason, S., and Jakob, C.: The Climatology, Meteorology, and Boundary Layer Structure of Marine Cold Air Outbreaks in Both Hemispheres, Journal of Climate, 29, 1999 – 2014, https://doi.org/10.1175/JCLI-D-15-0268.1, 2016.

Forsberg, R., Hvidegaard, S. M., Skourup, H., and Simonsen, S.: Three decades of polar airborne campaigns in the Arctic and Antarctica, in: AGU Fall Meeting Abstracts, vol. 2023 of *AGU Fall Meeting Abstracts*, pp. C31C–1365, 2023.

Geerts, B., Giangrande, S. E., McFarquhar, G. M., Xue, L., Abel, S. J., Comstock, J. M., Crewell, S., DeMott, P. J., Ebell, K., Field, P., Hill, T. C. J., Hunzinger, A., Jensen, M. P., Johnson, K. L., Juliano, T. W., Kollias, P., Kosovic, B., Lackner, C., Luke, E., Lüpkes, C., Matthews, A. A., Neggers, R., Ovchinnikov, M., Powers, H., Shupe, M. D., Spengler, T., Swanson, B. E., Tjernström, M., Theisen, A. K., Wales, N. A., Wang, Y., Wendisch, M., and Wu, P.: The COMBLE Campaign: A Study of Marine Boundary Layer Clouds in Arctic Cold-Air Outbreaks, Bulletin of the American Meteorological Society, 103, E1371 – E1389, https://doi.org/10.1175/BAMS-D-21-0044.1, 2022.

Gryschka, M. and Raasch, S.: Roll convection during a cold air outbreak: A large eddy simulation with stationary model domain, Geophysical Research Letters, 32, https://doi.org/10.1029/2005GL022872, 2005.

Heikenfeld, M., Marinescu, P. J., Christensen, M., Watson-Parris, D., Senf, F., van den Heever, S. C., and Stier, P.: tobac 1.2: towards a flexible framework for tracking and analysis of clouds in diverse datasets, Geoscientific Model Development, 12, 4551–4570, https://doi.org/10.5194/gmd-12-4551-2019, 2019.

Hersbach, H., Bell, B., Berrisford, P., Biavati, G., Horányi, A., Muñoz Sabater, J., Nicolas, J., Peubey, C., Radu, R., Rozum, I., Schepers, D., Simmons, A., Soci, C., Dee, D., and Thépaut, J.-N.: ERA5 hourly data on pressure levels from 1940 to present, https://doi.org/10.24381/cds.bd0915c6, accessed on 2025-04-03, 2023a.

Hersbach, H., Bell, B., Berrisford, P., Biavati, G., Horányi, A., Muñoz Sabater, J., Nicolas, J., Peubey, C., Radu, R., Rozum, I., Schepers, D., Simmons, A., Soci, C., Dee, D., and Thépaut, J.-N.: ERA5 hourly data on single levels from 1940 to present, https://doi.org/10.24381/cds.adbb2d47, accessed on 2025-04-03, 2023b.

Inoue, J., Sato, K., Rinke, A., Cassano, J. J., Fettweis, X., Heinemann, G., Matthes, H., Orr, A., Phillips, T., Seefeldt, M., Solomon, A., and Webster, S.: Clouds and Radiation Processes in Regional Climate Models Evaluated Using Observations Over the Ice-free Arctic Ocean, Journal of Geophysical Research: Atmospheres, 126, e2020JD033 904, https://doi.org/10.1029/2020JD033904, e2020JD033904 2020JD033904, 2021.

Kirbus, B., Schirmacher, I., Klingebiel, M., Schäfer, M., Ehrlich, A., Slättberg, N., Lucke, J., Moser, M., Müller, H., and Wendisch, M.: Thermodynamic and cloud evolution in a cold-air outbreak during HALO-$(AC)^3$: quasi-Lagrangian observations compared to the ERA5 and CARRA reanalyses, Atmospheric Chemistry and Physics, 24, 3883–3904, https://doi.org/10.5194/acp-24-3883-2024, 2024.

Kölling, T., Zinner, T., and Mayer, B.: Aircraft-based stereographic reconstruction of 3-D cloud geometry, Atmospheric Measurement Techniques, 12, 1155–1166, https://doi.org/10.5194/amt-12-1155-2019, 2019.

Komurcu, M., Storelvmo, T., Tan, I., Lohmann, U., Yun, Y., Penner, J. E., Wang, Y., Liu, X., and Takemura, T.: Intercomparison of the cloud water phase among global climate models, Journal of Geophysical Research: Atmospheres, 119, 3372–3400, https://doi.org/10.1002/2013JD021119, 2014.

Korolev, A. and Milbrandt, J.: How Are Mixed-Phase Clouds Mixed?, Geophysical Research Letters, 49, e2022GL099 578, https://doi.org/10.1029/2022GL099578, e2022GL099578 2022GL099578, 2022.

Korolev, A., McFarquhar, G., Field, P. R., Franklin, C., Lawson, P., Wang, Z., Williams, E., Abel, S. J., Axisa, D., Borrmann, S., Crosier, J., Fugal, J., Krämer, M., Lohmann, U., Schlenczek, O., Schnaiter, M., and Wendisch, M.: Mixed-Phase Clouds: Progress and Challenges, Meteorological Monographs, 58, 5.1 – 5.50, https://doi.org/10.1175/AMSMONOGRAPHS-D-17-0001.1, 2017.

Krautstrunk, M. and Giez, A.: The Transition From FALCON to HALO Era Airborne Atmospheric Research, pp. 609–624, Springer Berlin Heidelberg, Berlin, Heidelberg, https://doi.org/10.1007/978-3-642-30183-4_37, 2012.

Kretzschmar, J., Salzmann, M., Mülmenstädt, J., and Quaas, J.: Arctic clouds in ECHAM6 and their sensitivity to cloud microphysics and surface fluxes, Atmospheric Chemistry and Physics, 19, 10 571–10 589, https://doi.org/10.5194/acp-19-10571-2019, 2019.

Kretzschmar, J., Stapf, J., Klocke, D., Wendisch, M., and Quaas, J.: Employing airborne radiation and cloud microphysics observations to improve cloud representation in ICON at kilometer-scale resolution in the Arctic, Atmospheric Chemistry and Physics, 20, 13 145–13 165, https://doi.org/10.5194/acp-20-13145-2020, 2020.

Lackner, C. P., Geerts, B., Juliano, T. W., Xue, L., and Kosovic, B.: Vertical Structure of Clouds and Precipitation During Arctic Cold-Air Outbreaks and Warm-Air Intrusions: Observations From COMBLE, Journal of Geophysical Research: Atmospheres, 128, e2022JD038 403, https://doi.org/10.1029/2022JD038403, e2022JD038403 2022JD038403, 2023.

Lloyd, G., Choularton, T. W., Bower, K. N., Gallagher, M. W., Crosier, J., O'Shea, S., Abel, S. J., Fox, S., Cotton, R., and Boutle, I. A.: In situ measurements of cloud microphysical and aerosol properties during the break-up of stratocumulus cloud layers in cold air outbreaks over the North Atlantic, Atmospheric Chemistry and Physics, 18, 17 191–17 206, https://doi.org/10.5194/acp-18-17191-2018, 2018.

Ludwig, V., Spreen, G., and Pedersen, L. T.: Evaluation of a New Merged Sea-Ice Concentration Dataset at 1 km Resolution from Thermal Infrared and Passive Microwave Satellite Data in the Arctic, Remote Sensing, 12, https://doi.org/10.3390/rs12193183, 2020.

Mages, Z., Kollias, P., Zhu, Z., and Luke, E. P.: Surface-based observations of cold-air outbreak clouds during the COMBLE field campaign, Atmospheric Chemistry and Physics, 23, 3561–3574, https://doi.org/10.5194/acp-23-3561-2023, 2023.

Maherndl, N., Moser, M., Schirmacher, I., Bansemer, A., Lucke, J., Voigt, C., and Maahn, M.: How does riming influence the observed spatial variability of ice water in mixed-phase clouds?, Atmospheric Chemistry and Physics, 24, 13 935–13 960, https://doi.org/10.5194/acp-24-13935-2024, 2024.

Marchant, B., Platnick, S., Meyer, K., and Wind, G.: Evaluation of the MODIS Collection 6 multilayer cloud detection algorithm through comparisons with CloudSat Cloud Profiling Radar and CALIPSO CALIOP products, Atmospheric Measurement Techniques, 13, 3263–3275, https://doi.org/10.5194/amt-13-3263-2020, 2020.

Mateling, M. E., Pettersen, C., Kulie, M. S., and L'Ecuyer, T. S.: Marine Cold-Air Outbreak Snowfall in the North Atlantic: A CloudSat Perspective, Journal of Geophysical Research: Atmospheres, 128, e2022JD038 053, https://doi.org/10.1029/2022JD038053, e2022JD038053 2022JD038053, 2023.

Matus, A. V. and L'Ecuyer, T. S.: The role of cloud phase in Earth's radiation budget, Journal of Geophysical Research: Atmospheres, 122, 2559–2578, https://doi.org/10.1002/2016JD025951, 2017.

McCoy, D. T., Hartmann, D. L., Zelinka, M. D., Ceppi, P., and Grosvenor, D. P.: Mixed-phase cloud physics and Southern Ocean cloud feedback in climate models, Journal of Geophysical Research: Atmospheres, 120, 9539–9554, https://doi.org/10.1002/2015JD023603, 2015.

McCoy, I. L., Wood, R., and Fletcher, J. K.: Identifying Meteorological Controls on Open and Closed Mesoscale Cellular Convection Associated with Marine Cold Air Outbreaks, Journal of Geophysical Research: Atmospheres, 122, 11,678–11,702, https://doi.org/10.1002/2017JD027031, 2017.

Michaelis, J., Schmitt, A. U., Lüpkes, C., Hartmann, J., Birnbaum, G., and Vihma, T.: Observations of marine cold-air outbreaks: a comprehensive data set of airborne and dropsonde measurements from the Springtime Atmospheric Boundary Layer Experiment (STABLE), Earth System Science Data, 14, 1621–1637, https://doi.org/10.5194/essd-14-1621-2022, 2022.

Morrison, H., De Boer, G., Feingold, G., Harrington, J., Shupe, M., and Sulia, K.: Resilience of persistent Arctic mixed-phase clouds, Nature Geoscience, 5, 11–17, https://doi.org/10.1038/ngeo1332, 2012.

Moser, M., Lucke, J., De La Torre Castro, E., Mayer, J., and Voigt, C.: DLR in situ cloud measurements during HALO-$(AC)^3$ Arctic airborne campaign, https://doi.org/10.1594/PANGAEA.963247, 2023.

Murray-Watson, R. J., Gryspeerdt, E., and Goren, T.: Investigating the development of clouds within marine cold-air outbreaks, Atmospheric Chemistry and Physics, 23, 9365–9383, https://doi.org/10.5194/acp-23-9365-2023, 2023.

Otsu, N.: A Threshold Selection Method from Gray-Level Histograms, IEEE Transactions on Systems, Man, and Cybernetics, 9, 62–66, https://doi.org/10.1109/TSMC.1979.4310076, 1979.

Papritz, L. and Spengler, T.: A Lagrangian Climatology of Wintertime Cold Air Outbreaks in the Irminger and Nordic Seas and Their Role in Shaping Air–Sea Heat Fluxes, Journal of Climate, 30, 2717 – 2737, https://doi.org/10.1175/JCLI-D-16-0605.1, 2017.

Pithan, F., Medeiros, B., and Mauritsen, T.: Mixed-phase clouds cause climate model biases in Arctic wintertime temperature inversions, Climate Dynamics, https://doi.org/10.1007/s00382-013-1964-9, 2014.

Pithan, F., Ackerman, A., Angevine, W. M., Hartung, K., Ickes, L., Kelley, M., Medeiros, B., Sandu, I., Steeneveld, G.-J., Sterk, H. A. M., Svensson, G., Vaillancourt, P. A., and Zadra, A.: Select strengths and biases of models in representing the Arctic winter boundary layer over sea ice: the Larcform 1 single column model intercomparison, Journal of Advances in Modeling Earth Systems, 8, 1345–1357, https://doi.org/10.1002/2016MS000630, 2016.

Pithan, F., Svensson, G., Caballero, R., Chechin, D., Cronin, T. W., Ekman, A. M. L., Neggers, R., Shupe, M. D., Solomon, A., Tjernström, M., and Wendisch, M.: Role of air-mass transformations in exchange between the Arctic and mid-latitudes, Nature Geoscience, 11, 805–812, https://doi.org/10.1038/s41561-018-0234-1, 2018.

Pörtge, V., Kölling, T., Weber, A., Volkmer, L., Emde, C., Zinner, T., Forster, L., and Mayer, B.: High-spatial-resolution retrieval of cloud droplet size distribution from polarized observations of the cloudbow, Atmospheric Measurement Techniques, 16, 645–667, https://doi.org/10.5194/amt-16-645-2023, 2023.

Pörtge, V. T.: Understanding cloud droplet size distributions from multi-angle polarimetric observations, http://nbn-resolving.de/urn:nbn:de:bvb:19-340021, 2024.

Ruiz-Donoso, E., Ehrlich, A., Schäfer, M., Jäkel, E., Schemann, V., Crewell, S., Mech, M., Kulla, B. S., Kliesch, L.-L., Neuber, R., and Wendisch, M.: Small-scale structure of thermodynamic phase in Arctic mixed-phase clouds observed by airborne remote sensing during a cold air outbreak and a warm air advection event, Atmospheric Chemistry and Physics, 20, 5487–5511, https://doi.org/10.5194/acp-20-5487-2020, 2020.

Sato, Y., Miura, H., Yashiro, H., Goto, D., Takemura, T., Tomita, H., and Nakajima, T.: Unrealistically pristine air in the Arctic produced by current global scale models, Scientific Reports, 6, https://doi.org/10.1038/srep26561, 2016.

Schäfer, M., Bierwirth, E., Ehrlich, A., Jäkel, E., Werner, F., and Wendisch, M.: Directional, horizontal inhomogeneities of cloud optical thickness fields retrieved from ground-based and airbornespectral imaging, Atmospheric Chemistry and Physics, 17, 2359–2372, https://doi.org/10.5194/acp-17-2359-2017, 2017.

Schäfer, M., Loewe, K., Ehrlich, A., Hoose, C., and Wendisch, M.: Simulated and observed horizontal inhomogeneities of optical thickness of Arctic stratus, Atmospheric Chemistry and Physics, 18, 13 115–13 133, https://doi.org/10.5194/acp-18-13115-2018, 2018.

Schirmacher, I., Schnitt, S., Klingebiel, M., Maherndl, N., Kirbus, B., Ehrlich, A., Mech, M., and Crewell, S.: Clouds and precipitation in the initial phase of marine cold-air outbreaks as observed by airborne remote sensing, Atmospheric Chemistry and Physics, 24, 12 823–12 842, https://doi.org/10.5194/acp-24-12823-2024, 2024.

Seppala, H., Zhang, Z., and Zheng, X.: Developing a Lagrangian Frame Transformation on Satellite Data to Study Cloud Microphysical Transitions in Arctic Marine Cold Air Outbreaks, Geophysical Research Letters, 52, e2025GL115 637, https://doi.org/10.1029/2025GL115637, e2025GL115637 2025GL115637, 2025.

Shupe, M. D., Rex, M., Blomquist, B., Persson, P. O. G., Schmale, J., Uttal, T., Althausen, D., Angot, H., Archer, S., Bariteau, L., Beck, I., Bilberry, J., Bucci, S., Buck, C., Boyer, M., Brasseur, Z., Brooks, I. M., Calmer, R., Cassano, J., Castro, V., Chu, D., Costa, D., Cox, C. J., Creamean, J., Crewell, S., Dahlke, S., Damm, E., de Boer, G., Deckelmann, H., Dethloff, K., Dütsch, M., Ebell, K., Ehrlich, A., Ellis, J., Engelmann, R., Fong, A. A., Frey, M. M., Gallagher, M. R., Ganzeveld, L., Gradinger, R., Graeser, J., Greenamyer, V., Griesche, H., Griffiths, S., Hamilton, J., Heinemann, G., Helmig, D., Herber, A., Heuzé, C., Hofer, J., Houchens, T., Howard, D., Inoue, J., Jacobi, H.-W., Jaiser, R., Jokinen, T., Jourdan, O., Jozef, G., King, W., Kirchgaessner, A., Klingebiel, M., Krassovski, M., Krumpen, T., Lampert, A., Landing, W., Laurila, T., Lawrence, D., Lonardi, M., Loose, B., Lüpkes, C., Maahn, M., Macke, A., Maslowski, W., Marsay, C., Maturilli, M., Mech, M., Morris, S., Moser, M., Nicolaus, M., Ortega, P., Osborn, J., Pätzold, F., Perovich, D. K., Petäjä, T., Pilz, C., Pirazzini, R., Posman, K., Powers, H., Pratt, K. A., Preußer, A., Quéléver, L., Radenz, M., Rabe, B., Rinke, A., Sachs, T., Schulz, A., Siebert, H., Silva, T., Solomon, A., Sommerfeld, A., Spreen, G., Stephens, M., Stohl, A., Svensson, G., Uin, J., Viegas, J., Voigt, C., von der Gathen, P., Wehner, B., Welker, J. M., Wendisch, M., Werner, M., Xie, Z., and Yue, F.: Overview of the MOSAiC expedition: Atmosphere, Elementa: Science of the Anthropocene, 10, 00 060, https://doi.org/10.1525/elementa.2021.00060, 2022.

Smith, D. M., Screen, J. A., Deser, C., Cohen, J., Fyfe, J. C., García-Serrano, J., Jung, T., Kattsov, V., Matei, D., Msadek, R., Peings, Y., Sigmond, M., Ukita, J., Yoon, J.-H., and Zhang, X.: The Polar Amplification Model Intercomparison Project (PAMIP) contribution to CMIP6: investigating the causes and consequences of polar amplification, Geoscientific Model Development, 12, 1139–1164, https://doi.org/10.5194/gmd-12-1139-2019, 2019.

Sokolowsky, G. A., Freeman, S. W., Jones, W. K., Kukulies, J., Senf, F., Marinescu, P. J., Heikenfeld, M., Brunner, K. N., Bruning, E. C., Collis, S. M., Jackson, R. C., Leung, G. R., Pfeifer, N., Raut, B. A., Saleeby, S. M., Stier, P., and van den Heever, S. C.: *tobac* v1.5: introducing fast 3D tracking, splits and mergers, and other enhancements for identifying and analysing meteorological phenomena, Geoscientific Model Development, 17, 5309–5330, https://doi.org/10.5194/gmd-17-5309-2024, 2024.

Spensberger, C. and Spengler, T.: Sensitivity of Air-Sea Heat Exchange in Cold-Air Outbreaks to Model Resolution and Sea-Ice Distribution, Journal of Geophysical Research: Atmospheres, 126, e2020JD033 610, https://doi.org/https://doi.org/10.1029/2020JD033610, e2020JD033610 2020JD033610, 2021.

Sprenger, M. and Wernli, H.: The LAGRANTO Lagrangian analysis tool – version 2.0, Geoscientific Model Development, 8, 2569–2586, https://doi.org/10.5194/gmd-8-2569-2015, 2015.

Stevens, B., Ament, F., Bony, S., Crewell, S., Ewald, F., Gross, S., Hansen, A., Hirsch, L., Jacob, M., Kölling, T., Konow, H., Mayer, B., Wendisch, M., Wirth, M., Wolf, K., Bakan, S., Bauer-Pfundstein, M., Brueck, M., Delanoë, J., Ehrlich, A., Farrell, D., Forde, M., Gödde, F., Grob, H., Hagen, M., Jäkel, E., Jansen, F., Klepp, C., Klingebiel, M., Mech, M., Peters, G., Rapp, M., Wing, A. A., and Zinner, T.: A High-Altitude Long-Range Aircraft Configured as a Cloud Observatory: The NARVAL Expeditions, Bulletin of the American Meteorological Society, 100, 1061 – 1077, https://doi.org/10.1175/BAMS-D-18-0198.1, 2019.

Svingen, K., Brakstad, A., Våge, K., von Appen, W.-J., and Papritz, L.: The Impact of Cold-Air Outbreaks and Oceanic Lateral Fluxes on Dense-Water Formation in the Greenland Sea from a 10-Year Moored Record (1999–2009), Journal of Physical Oceanography, 53, 1499 – 1517, https://doi.org/10.1175/JPO-D-22-0160.1, 2023.

Tan, I. and Storelvmo, T.: Evidence of Strong Contributions From Mixed-Phase Clouds to Arctic Climate Change, Geophysical Research Letters, 46, 2894–2902, https://doi.org/10.1029/2018GL081871, 2019.

Tomassini, L., Field, P. R., Honnert, R., Malardel, S., McTaggart-Cowan, R., Saitou, K., Noda, A. T., and Seifert, A.: The "Grey Zone" cold air outbreak global model intercomparison: A cross evaluation using large-eddy simulations, Journal of Advances in Modeling Earth Systems, 9, 39–64, https://doi.org/10.1002/2016MS000822, 2017.

Tornow, F., Ackerman, A. S., and Fridlind, A. M.: Preconditioning of overcast-to-broken cloud transitions by riming in marine cold air outbreaks, Atmospheric Chemistry and Physics, 21, 12 049–12 067, https://doi.org/10.5194/acp-21-12049-2021, 2021.

Tornow, F., Ackerman, A. S., Fridlind, A. M., Tselioudis, G., Cairns, B., Painemal, D., and Elsaesser, G.: On the Impact of a Dry Intrusion Driving Cloud-Regime Transitions in a Midlatitude Cold-Air Outbreak, Journal of the Atmospheric Sciences, 80, 2881 – 2896, https://doi.org/10.1175/JAS-D-23-0040.1, 2023.

Uttal, T., Curry, J. A., McPhee, M. G., Perovich, D. K., Moritz, R. E., Maslanik, J. A., Guest, P. S., Stern, H. L., Moore, J. A., Turenne, R., Heiberg, A., Serreze, M. C., Wylie, D. P., Persson, O. G., Paulson, C. A., Halle, C., Morison, J. H., Wheeler, P. A., Makshtas, A., Welch, H., Shupe, M. D., Intrieri, J. M., Stamnes, K., Lindsey, R. W., Pinkel, R., Pegau, W. S., Stanton, T. P., and Grenfeld, T. C.: Surface Heat Budget of the Arctic Ocean, Bulletin of the American Meteorological Society, 83, 255 – 276, https://doi.org/10.1175/1520-0477(2002)083<0255:SHBOTA>2.3.CO;2, 2002.

Volkmer, L., Pörtge, V., Jakub, F., and Mayer, B.: Model-based evaluation of cloud geometry and droplet size retrievals from two-dimensional polarized measurements of specMACS, Atmospheric Measurement Techniques, 17, 1703–1719, https://doi.org/10.5194/amt-17-1703-2024, 2024.

Walbröl, A., Michaelis, J., Becker, S., Dorff, H., Ebell, K., Gorodetskaya, I., Heinold, B., Kirbus, B., Lauer, M., Maherndl, N., Maturilli, M., Mayer, J., Müller, H., Neggers, R. A. J., Paulus, F. M., Röttenbacher, J., Rückert, J. E., Schirmacher, I., Slättberg, N., Ehrlich, A., Wendisch, M., and Crewell, S.: Contrasting extremely warm and long-lasting cold air anomalies in the North Atlantic sector of the Arctic during the HALO-($\mathcal{AC}$)$^3$ campaign, Atmospheric Chemistry and Physics, 24, 8007–8029, https://doi.org/10.5194/acp-24-8007-2024, 2024.

Weber, A.: Remote sensing of mixed-phase clouds and their evolution during marine cold air outbreaks in the Arctic, https://doi.org/10.5282/edoc.36417, 2025.

Weber, A., Kölling, T., Pörtge, V., Baumgartner, A., Rammeloo, C., Zinner, T., and Mayer, B.: Polarization upgrade of specMACS: calibration and characterization of the 2D RGB polarization-resolving cameras, Atmospheric Measurement Techniques, 17, 1419–1439, https://doi.org/10.5194/amt-17-1419-2024, 2024.

Weber, A., Pörtge, V., Zinner, T., and Mayer, B.: Spectral radiance measurements with the hyperspectral and polarized imaging system specMACS during the HALO-(AC)3 field campaign, https://doi.org/10.1594/PANGAEA.966992, 2024.

Weber, A., Hoffmann, F., and Mayer, B.: Quasi-Lagrangian observations of cloud transitions during the initial phase of marine cold air outbreaks in the Arctic – Part 2: Vertical cloud structure, EGUsphere, 2025, 1–26, https://doi.org/10.5194/egusphere-2025-5832, 2025a.

Weber, A., Pörtge, V., Emde, C., and Mayer, B.: Retrieval of cloud thermodynamic phase partitioning from multi-angle polarimetric imaging of Arctic mixed-phase clouds, EGUsphere, 2025, 1–28, https://doi.org/10.5194/egusphere-2025-3595, 2025b.

Wendisch, M., Handorf, D., Tegen, I., Neggers, R. A. J., and Spreen, G.: Glimpsing the Ins and Outs of the Arctic Atmospheric Cauldron, Eos, 102, https://doi.org/10.1029/2021EO155959, 2021.

Wendisch, M., Brückner, M., Crewell, S., Ehrlich, A., Notholt, J., Lüpkes, C., Macke, A., Burrows, J. P., Rinke, A., Quaas, J., Maturilli, M., Schemann, V., Shupe, M. D., Akansu, E. F., Barrientos-Velasco, C., Bärfuss, K., Blechschmidt, A.-M., Block, K., Bougoudis, I., Bozem, H., Böckmann, C., Bracher, A., Bresson, H., Bretschneider, L., Buschmann, M., Chechin, D. G., Chylik, J., Dahlke, S., Deneke, H., Dethloff, K., Donth, T., Dorn, W., Dupuy, R., Ebell, K., Egerer, U., Engelmann, R., Eppers, O., Gerdes, R., Gierens, R., Gorodetskaya, I. V., Gottschalk, M., Griesche, H., Gryanik, V. M., Handorf, D., Harm-Altstädter, B., Hartmann, J., Hartmann, M., Heinold, B., Herber, A., Herrmann, H., Heygster, G., Höschel, I., Hofmann, Z., Hölemann, J., Hünerbein, A., Jafariserajehlou, S., Jäkel, E., Jacobi, C., Janout, M., Jansen, F., Jourdan, O., Jurányi, Z., Kalesse-Los, H., Kanzow, T., Käthner, R., Kliesch, L. L., Klingebiel, M., Knudsen, E. M., Kovács, T., Körtke, W., Krampe, D., Kretzschmar, J., Kreyling, D., Kulla, B., Kunkel, D., Lampert, A., Lauer, M., Lelli, L., von Lerber, A., Linke, O., Löhnert, U., Lonardi, M., Losa, S. N., Losch, M., Maahn, M., Mech, M., Mei, L., Mertes, S., Metzner, E., Mewes, D., Michaelis, J., Mioche, G., Moser, M., Nakoudi, K., Neggers, R., Neuber, R., Nomokonova, T., Oelker, J., Papakonstantinou-Presvelou, I., Pätzold, F., Pefanis, V., Pohl, C., van Pinxteren, M., Radovan, A., Rhein, M., Rex, M., Richter, A., Risse, N., Ritter, C., Rostosky, P., Rozanov, V. V., Donoso, E. R., Garfias, P. S., Salzmann, M., Schacht, J., Schäfer, M., Schneider, J., Schnierstein, N., Seifert, P., Seo, S., Siebert, H., Soppa, M. A., Spreen, G., Stachlewska, I. S., Stapf, J., Stratmann, F., Tegen, I., Viceto, C., Voigt, C., Vountas, M., Walbröl, A., Walter, M., Wehner, B., Wex, H., Willmes, S., Zanatta, M., and Zeppenfeld, S.: Atmospheric and Surface Processes, and Feedback Mechanisms Determining Arctic Amplification: A Review of First Results and Prospects of the (AC)3 Project, Bulletin of the American Meteorological Society, 104, E208 – E242, https://doi.org/10.1175/BAMS-D-21-0218.1, 2023.

Wendisch, M., Crewell, S., Ehrlich, A., Herber, A., Kirbus, B., Lüpkes, C., Mech, M., Abel, S. J., Akansu, E. F., Ament, F., Aubry, C., Becker, S., Borrmann, S., Bozem, H., Brückner, M., Clemen, H.-C., Dahlke, S., Dekoutsidis, G., Delanoë, J., De La Torre Castro, E., Dorff, H., Dupuy, R., Eppers, O., Ewald, F., George, G., Gorodetskaya, I. V., Grawe, S., Groß, S., Hartmann, J., Henning, S., Hirsch, L., Jäkel, E., Joppe, P., Jourdan, O., Jurányi, Z., Karalis, M., Kellermann, M., Klingebiel, M., Lonardi, M., Lucke, J., Luebke, A. E., Maahn, M., Maherndl, N., Maturilli, M., Mayer, B., Mayer, J., Mertes, S., Michaelis, J., Michalkov, M., Mioche, G., Moser, M., Müller, H., Neggers, R., Ori, D., Paul, D., Paulus, F. M., Pilz, C., Pithan, F., Pöhlker, M., Pörtge, V., Ringel, M., Risse, N., Roberts, G. C., Rosenburg, S., Röttenbacher, J., Rückert, J., Schäfer, M., Schaefer, J., Schemann, V., Schirmacher, I., Schmidt, J., Schmidt, S., Schneider, J., Schnitt, S., Schwarz, A., Siebert, H., Sodemann, H., Sperzel, T., Spreen, G., Stevens, B., Stratmann, F., Svensson, G., Tatzelt, C., Tuch, T., Vihma, T., Voigt, C., Volkmer, L., Walbröl, A., Weber, A., Wehner, B., Wetzel, B., Wirth, M., and Zinner, T.: Overview: quasi-Lagrangian observations of Arctic air mass transformations – introduction and initial results of the HALO–$(\mathcal{AC})^3$ aircraft campaign, Atmospheric Chemistry and Physics, 24, 8865–8892, https://doi.org/10.5194/acp-24-8865-2024, 2024.

Wendisch, M., Kirbus, B., Ori, D., Shupe, M. D., Crewell, S., Sodemann, H., and Schemann, V.: Observed and modeled Arctic air-mass transformations during warm air intrusions and cold air outbreaks, Atmospheric Chemistry and Physics, 25, 15 047–15 076, https://doi.org/10.5194/acp-25-15047-2025, 2025.

Wesche, C., Steinhage, D., and Nixdorf, U.: Polar aircraft Polar5 and Polar6 operated by the Alfred Wegener Institute, Journal of large-scale research facilities, 2, A87, https://doi.org/http://dx.doi.org/10.17815/jlsrf-2-153, 2016.

Wu, P. and Ovchinnikov, M.: Cloud Morphology Evolution in Arctic Cold-Air Outbreak: Two Cases During COMBLE Period, Journal of Geophysical Research: Atmospheres, 127, e2021JD035 966, https://doi.org/10.1029/2021JD035966, e2021JD035966 2021JD035966, 2022.

Xia, Z. and McFarquhar, G. M.: Dependence of Cloud Macrophysical Properties and Phase Distributions on Environmental Conditions Over the North Atlantic and Southern Ocean: Results From COMBLE and MARCUS, Journal of Geophysical Research: Atmospheres, 129, e2023JD039 869, https://doi.org/10.1029/2023JD039869, e2023JD039869 2023JD039869, 2024.

Young, G., Jones, H. M., Choularton, T. W., Crosier, J., Bower, K. N., Gallagher, M. W., Davies, R. S., Renfrew, I. A., Elvidge, A. D., Darbyshire, E., Marenco, F., Brown, P. R. A., Ricketts, H. M. A., Connolly, P. J., Lloyd, G., Williams, P. I., Allan, J. D., Taylor, J. W., Liu, D., and Flynn, M. J.: Observed microphysical changes in Arctic mixed-phase clouds when transitioning from sea ice to open ocean, Atmospheric Chemistry and Physics, 16, 13 945–13 967, https://doi.org/10.5194/acp-16-13945-2016, 2016.